nature cell biology

ARTICLES

https://doi.org/10.1038/s41556-018-0178-0

BAP1 links metabolic regulation of ferroptosis to tumour suppression

Yilei Zhang[1,10], Jiejun Shi[2,10], Xiaoguang Liu[1], Li Feng[3], Zihua Gong[1,4], Pranavi Koppula[1,5], Kapil Sirohi[1], Xu Li[1,8], Yongkun Wei[6], Hyemin Lee[1], Li Zhuang[1], Gang Chen[3], Zhen-Dong Xiao[1,9], Mien-Chie Hung[5,6,7], Junjie Chen[1,5], Peng Huang[3,5], Wei Li[2*] and Boyi Gan[1,5,6*]

The roles and regulatory mechanisms of ferroptosis (a non-apoptotic form of cell death) in cancer remain unclear. The tumour suppressor BRCA1-associated protein 1 (*BAP1*) encodes a nuclear deubiquitinating enzyme to reduce histone 2A ubiquitination (H2Aub) on chromatin. Here, integrated transcriptomic, epigenomic and cancer genomic analyses link BAP1 to metabolism-related biological processes, and identify cystine transporter *SLC7A11* as a key BAP1 target gene in human cancers. Functional studies reveal that BAP1 decreases H2Aub occupancy on the *SLC7A11* promoter and represses *SLC7A11* expression in a deubiquitinating-dependent manner, and that BAP1 inhibits cystine uptake by repressing *SLC7A11* expression, leading to elevated lipid peroxidation and ferroptosis. Furthermore, we show that BAP1 inhibits tumour development partly through SLC7A11 and ferroptosis, and that cancer-associated *BAP1* mutants lose their abilities to repress *SLC7A11* and to promote ferroptosis. Together, our results uncover a previously unappreciated epigenetic mechanism coupling ferroptosis to tumour suppression.

To survive, cancer cells require an adequate supply of nutrients, such as amino acids, to maintain redox homeostasis and to meet their biosynthetic and bioenergetic needs[1,2]. Nutrient depletion induces metabolic stress and eventually provokes cell death, including apoptosis and other non-apoptotic forms of regulated cell death[3,4]. Cancer cells engage strategies of metabolic adaptation, including inactivation of apoptosis pathways, to survive under metabolic stress conditions and to allow tumour progression[5,6]. It is conceivable that non-apoptotic cell death pathways are also dysregulated in cancer, although the underlying mechanisms remain much less understood.

Ferroptosis is a recently identified metabolic stress-induced non-apoptotic form of regulated cell death that is caused by cystine depletion and overproduction of lipid-based reactive oxygen species (ROS), particularly lipid hydroperoxide, in an iron-dependent manner[7–11]. Solute carrier family 7 member 11 (SLC7A11, also called xCT), the catalytic subunit of the cystine/glutamate antiporter system x_c^-, is the major transporter of extracellular cystine[12–14]. Correspondingly, cystine depletion or drugs that block SLC7A11-mediated cystine uptake, such as erastin, induce ferroptosis[7]. Intracellular cystine is rapidly converted to cysteine, which subsequently serves as the rate-limiting precursor for glutathione synthesis. Glutathione peroxidase 4 (GPX4) utilizes reduced glutathione (GSH) to reduce lipid hydroperoxides to lipid alcohols, to protect cells against membrane lipid peroxidation and inhibit ferroptosis[15,16]. Ferroptosis is morphologically, genetically and biochemically distinct from other forms of regulated cell death, such as apoptosis and necroptosis[7]. It is well established that cell death, most notably apoptosis, plays important roles in tumour suppression[17,18]. However, the roles and regulatory mechanisms of ferroptosis in tumour biology remain largely unexplored.

BRCA1-associated protein 1 (*BAP1*) encodes a nuclear deubiquitinating (DUB) enzyme that interacts with several transcriptional factors and chromatin-modifying enzymes, such as FOXK1/2, ASXL1/2, OGT, HCFC1 and KDM1B, and plays an important role in the epigenetic regulation of gene transcription[19–25]. BAP1 and its associated proteins form the polycomb repressive deubiquitinase (PR–DUB) complex, which mainly functions to remove monoubiquitin from ubiquitinated histone 2A at lysine 119 (H2Aub)[26]. It has been shown that this type of histone modification regulates gene transcription through epigenetic mechanisms[27–29]. *BAP1* is a tumour suppressor gene with frequent inactivating mutations and deletions in a variety of sporadic human cancers, including uveal melanoma (UVM), renal cell carcinoma, mesothelioma and cholangiocarcinoma[19,30–33]. However, the mechanisms by which BAP1 exerts its tumour suppression function, particularly the extent to which BAP1 regulation of H2Aub levels on chromatin and corresponding transcriptional targets plays a role in its tumour suppression function, remain unclear. In this study, we conduct integrative analyses to achieve a comprehensive identification of BAP1-regulated target genes and relevant biological processes in cancer cells, and identify a BAP1-mediated epigenetic mechanism that links ferroptosis to tumour suppression.

Results

Genome-wide analyses link BAP1 to metabolism-related biological processes. We conducted unbiased genome-wide analyses to characterize BAP1-dependent H2Aub occupancies and corresponding

[1]Department of Experimental Radiation Oncology, The University of Texas MD Anderson Cancer Center, Houston, TX, USA. [2]Division of Biostatistics, Dan L. Duncan Cancer Center and Department of Molecular and Cellular Biology, Baylor College of Medicine, Houston, TX, USA. [3]Department of Translational Molecular Pathology, The University of Texas MD Anderson Cancer Center, Houston, TX, USA. [4]Department of Cancer Biology, Cleveland Clinic Lerner Research Institute, Cleveland, OH, USA. [5]The University of Texas MD Anderson UT Health Graduate School of Biomedical Sciences, Houston, TX, USA. [6]Department of Molecular and Cellular Oncology, The University of Texas MD Anderson Cancer Center, Houston, TX, USA. [7]Graduate Institute of Biomedical Sciences and Center for Molecular Medicine, China Medical University, Taichung, Taiwan. [8]Present address: Institute of Biology, Westlake University, Hangzhou, Zhejiang Province, China. [9]Present address: Guangdong Key Laboratory of Liver Disease Research, The Third Affiliated Hospital of Sun Yat-Sen University, Guangzhou, China. [10]These authors contributed equally: Yilei Zhang, Jiejun Shi. *e-mail: WL1@bcm.edu; bgan@mdanderson.org

transcriptional alterations in the genome. To this end, we established UMRC6 cells (a *BAP1*-deficient renal cancer cell line) with stable expression of an empty vector (EV), *BAP1* wild type (WT) and a *BAP1* C91A DUB-inactive mutant[34]. We confirmed that re-expression of BAP1 WT, but not its C91A mutant, in UMRC6 cells decreased global H2Aub levels (Fig. 1a). We then performed H2Aub chromatin immunoprecipitation coupled with high-throughput sequencing (ChIP–seq) analyses in these cells. Our ChIP–seq analyses revealed that re-expression of *BAP1* WT, but not its C91A mutant, resulted in significant reduction of genome-wide H2Aub occupancies in UMRC6 cells (Fig. 1b,c). Distribution analysis showed that more than half of H2Aub bindings in EV/WT/C91A cells were detected at promoter or gene body regions (Supplementary Fig. 1a). *BAP1* WT, but not *BAP1* C91A, cells showed decreases of H2Aub occupancies at promoter, gene body and intergenic regions (Fig. 1d and Supplemenary Fig. 1b). Overall, we identified more than 5,000 genes with reduced H2Aub occupancies in *BAP1* WT cells compared with EV cells (Fig. 1e; false discovery rate (FDR) < 0.001).

Parallel RNA sequencing (RNA–seq) analysis identified around 1,700 differentially expressed genes (983 upregulated genes and 717 downregulated genes) on *BAP1* re-expression in UMRC6 cells (Supplementary Fig. 1c; fold change > 1.5, FDR < 0.05). Integration of both H2Aub ChIP–seq and RNA–seq data sets identified 354 BAP1-upregulated genes and 187 BAP1-downregulated genes with BAP1-dependent H2Aub reduction in both gene sets (Fig. 1f and Supplementary Table 1). The current model proposes that H2Aub is associated with transcriptional repression[28], which would predict that BAP1-dependent H2Aub reduction correlates with BAP1-mediated transcriptional activation. To test this hypothesis, we conducted gene set enrichment analysis (GSEA) on the genes with different fold changes in BAP1-dependent H2Aub reduction (5,837 genes whose H2Aub levels were reduced by BAP1 >1.6-fold, 1,494 genes >2-fold, and 101 genes >2.5-fold). GSEA revealed, in all three analyses, that genes with BAP1-dependent H2Aub reduction were enriched with BAP1-upregulated genes; indeed, the more stringent the cutoff we used, the more significant the correlation (see Fig. 1g for 101 genes, normalized enrichment score = 1.61, FDR = 0; see Supplementary Fig. 1d for 1,494 genes, normalized enrichment score = 1.52, FDR = 0; see Supplementary Fig. 1e for 5,837 genes, normalized enrichment score = 1.22, FDR = 0). Thus, our analysis was consistent with the prevailing model that H2Aub correlates with transcriptional repression[28]. It is also worth noting that the fold changes in H2Aub binding on promoters of the genes that were differentially regulated by BAP1 were more pronounced than those in the total set of 5,837 genes (Fig. 1d,h,i and Supplementary Fig. 1b,f,g; with the following median $\log_2$-fold change of H2Aub on BAP1 re-expression: −0.44 for all 5,837 genes versus −1.03 for BAP1-downregulated genes versus −0.96 for BAP1-upregulated genes). Thus, BAP1-dependent H2Aub de-ubiquitination correlates with BAP1-mediated transcriptional alteration. Heatmap analysis of the H2Aub profile around transcriptional start sites (TSSs) revealed that the genes that were upregulated or downregulated by BAP1 displayed reduced H2Aub signals centred on TSSs on re-expression of *BAP1* WT, but not C91A (Fig. 1j).

Gene ontology (GO) analysis of 354 BAP1-upregulated and 187 BAP1-downregulated genes revealed that, while BAP1-upregulated genes were enriched in diverse cellular processes (Supplementary Fig. 1h and Supplementary Table 1), the genes that were downregulated by BAP1 showed striking enrichment in metabolism-related biological processes, among which 'response to oxidative stress' was the most significantly enriched (Fig. 1k and Supplementary Table 1). Together, our genome-wide analyses suggested that BAP1-mediated de-ubiquitination of H2Aub is associated with both transcriptional activation and repression of gene targets involved in different biological processes (see Discussion), and linked BAP1-repressed genes to metabolism.

Cancer genomic analyses link SLC7A11 to BAP1-mediated tumour suppression in human cancers. Next, we studied the potential relevance of BAP1-regulated genes to BAP1-mediated tumour suppression in human cancers through analysis of The Cancer Genome Atlas (TCGA) data sets. Because we conducted our genome-wide analyses in a renal cancer cell line, we focused on the TCGA Kidney Clear Cell Carcinoma (KIRC) data set[35] in our initial analysis. Specifically, we subjected the list of 541 genes (187 BAP1-downregulated and 354 BAP1-upregulated genes with reduced H2Aub occupancies; Fig. 1f) to a series of computational analyses, including (1) expression correlation with *BAP1* in KIRC, (2) comparison of expression in KIRC and normal kidneys and (3) patient survival prediction in KIRC (Fig. 2a). We aimed to identify BAP1-downregulated target genes (1) whose expression is inversely correlated with that of BAP1 in KIRC, (2) that are upregulated in KIRC compared with normal kidneys, and (3) whose upregulation correlates with shorter patient survival, and vice versa. Such analyses identified 20 BAP1-downregulated and 26 BAP1-upregulated genes that satisfied all three criteria, among which *SLC7A11* was the only downregulated gene, whereas *Shroom3* and *PARD3B* were the upregulated genes that showed statistical significance in all three analyses (Supplementary Table 2). Notably, *SLC7A11* was among the top genes identified in our RNA–seq and H2Aub ChIP–seq analyses (Fig. 1j and Supplementary Fig. 1c), and also among the genes involved in 'response to oxidative stress', the most significantly enriched biological process of BAP1-downregulated genes from the GO analysis (Supplementary Table 1). We therefore focused on SLC7A11 in the follow-up studies.

As shown in Fig. 2b-d, our analyses revealed that *SLC7A11* expression inversely correlated with *BAP1* expression in KIRC, that *SLC7A11* exhibited higher expression in KIRC than in normal kidneys, and that higher expression of *SLC7A11* predicted shorter survival in KIRC patients. We then extended the same analyses of *SLC7A11* to other TCGA data sets. Such analyses revealed that *BAP1* expression inversely correlated with *SLC7A11* expression not only in KIRC, but also in several other human cancers, including kidney papillary cell carcinoma (KIRP), UVM, pheochromocytoma and paraganglioma (PCPG) and breast invasive carcinoma (BRCA)[36–39] (Fig. 2e). Consistent with this, we observed an inverse correlation between BAP1 and SLC7A11 levels across a panel of cancer cell lines (Fig. 2f). Further comparison of the expression levels of *SLC7A11* in KIRP, PCPG, BRCA and corresponding normal tissues showed that *SLC7A11* is upregulated in these cancers (Fig. 2g). (Note that there was no normal tissue control for UVM in the TCGA or GTEx databases, so we were unable to conduct the analysis for UVM.) Correspondingly, *BAP1* is mutated/deleted (in UVM, KIRC and KIRP) or downregulated (in PCPG and BRCA) in these tumour types with *SLC7A11* high expression (Fig. 2h,i). Finally, we showed that, in KIRP and UVM, patients with high *SLC7A11* expression had shorter overall survival than did patients with low *SLC7A11* expression, whereas UVM patients with lower *BAP1* expression had significantly shorter overall survival (Fig. 2j-l). In KIRP and UVM, the combination of high *SLC7A11* and low *BAP1* expression predicted even worse clinical outcomes than either parameter alone (Fig. 2m,n). Together, our analyses identified *SLC7A11* as one of the most relevant target genes in BAP1-mediated tumour suppression in human cancers, and revealed that *BAP1* and *SLC7A11* expression levels show an inverse correlation and predict clinical outcomes in human cancers.

BAP1 suppresses *SLC7A11* expression and reduces H2Aub occupancy on the *SLC7A11* promoter. The aforementioned computational analyses prompted detailed mechanistic studies on how BAP1 regulates SLC7A11. UMRC6 cells, the *BAP1*-deficient cell line used in our RNA–seq and H2Aub ChIP–seq analyses, exhibited high SLC7A11 expression (Fig. 2f). We confirmed that

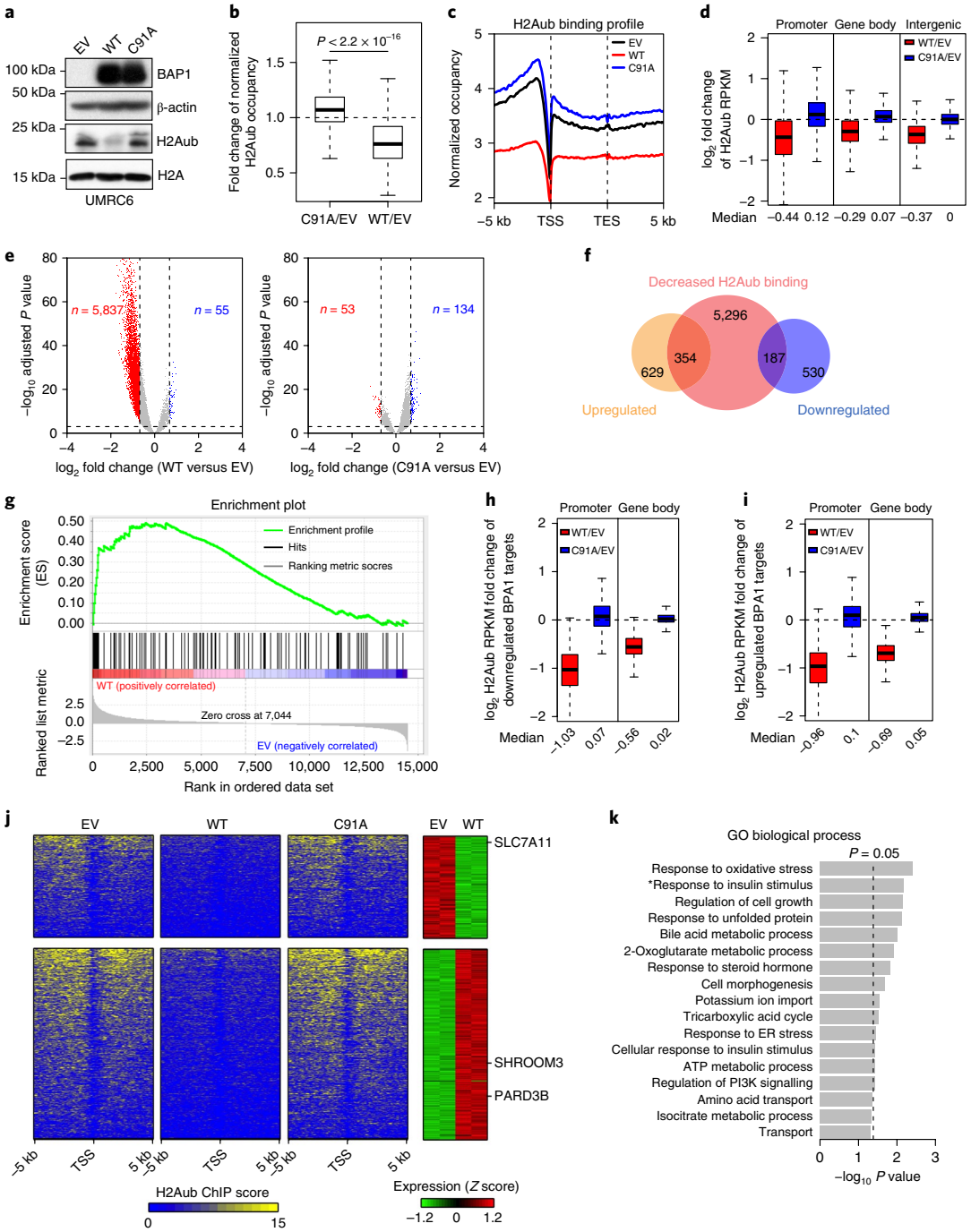

Fig. 1 | Genome-wide analyses link BAP1 to metabolism-related biological processes. a, Restoring *BAP1* WT but not C91A in UMRC6 cells decreased H2Aub level. The experiment was repeated four times, independently, with similar results. **b**, Box plot showing fold changes of H2Aub occupancies in *BAP1* WT or C91A compared with empty vector (EV) cells. Two-tailed unpaired Student's *t*-test. $n = 24{,}648$ counts of promoter whose H2Aub occupancy (RPKM) is higher than 0.5 in all three samples. **c**, Average genome-wide occupancies of H2Aub in indicated cells. TSS, transcription start site; TES, transcription end site. **d**, Box plots of the $\log_2$ fold changes of H2Aub occupancies in promoter, gene body and intergenic regions in *BAP1* WT or C91A compared with EV cells. $n = 25{,}772$ for promoter and gene body, which is the total gene count in the human reference. Total number of intergenic regions, $n = 14{,}237$. **e**, Volcano plots of H2Aub ChIP–seq data for *BAP1* WT or C91A compared with EV cells. Red and blue dots represent genes with at least 1.6-fold decrease or increase of H2Aub occupancies in *BAP1* WT (left) or C91A (right) compared with EV cells. **f**, Venn diagram showing overlap between 5,837 genes with decreased H2Aub occupancies and 1,700 differentially expressed genes (Fold change > 1.5, FDR < 0.05) on restoring *BAP1* in UMRC6 cells. **g**, GSEA showing that the 101 genes with >2.5-fold H2Aub reduction were positively enriched in BAP1-upregulated genes. **h**,**i**, Box plots of $\log_2$-fold changes of H2Aub occupancies in promoter and gene body regions for 187 genes (**h**) and 354 genes (**i**), as shown in **f**. **j**, Left three panels, Heatmaps showing the H2Aub profile around the TSS of 187 downregulated and 354 upregulated genes (**f**) in EV, *BAP1* WT and C91A cells, in decreasing order. Right panel, Heatmap showing expression levels of the corresponding genes in EV and *BAP1* WT cells. **k**, GO analysis for the 187 downregulated genes. Top annotation clusters are shown according to their enrichment scores ($-\log_{10}$(*P* value)). *Positive regulation of glucose import in response to insulin stimulus. Fisher's exact test. Box and whisker plots show centre line at median, box limits at 25th/75th centiles and whiskers ±1.5× interquartile range (IQR). Unprocessed blots are presented in Supplementary Fig. 7.

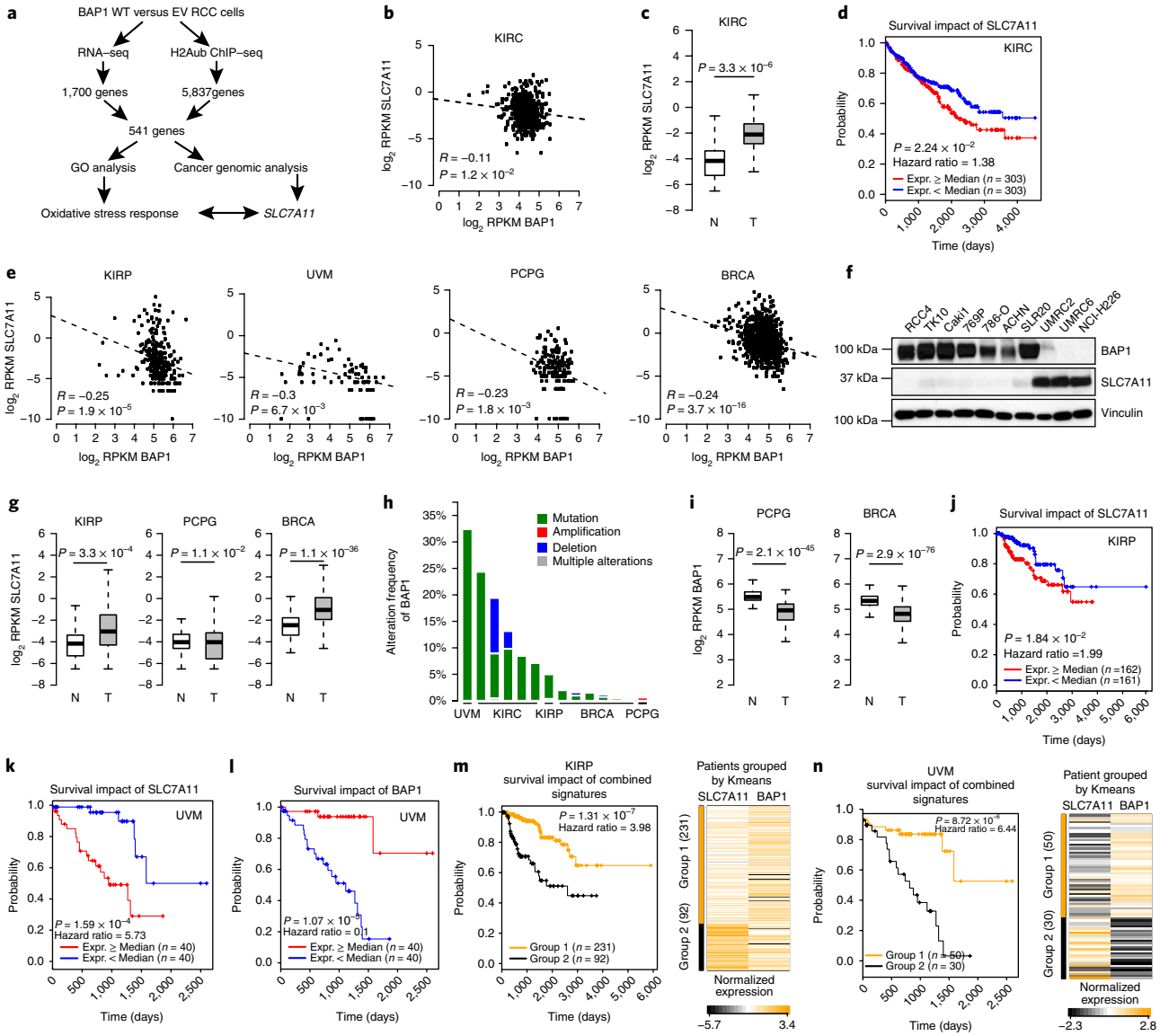

Fig. 2 | Cancer genomic analyses link SLC7A11 to BAP1-mediated tumour suppression in human cancers. a, Pipeline for identifying relevant BAP1 target genes in cancer. **b**,**e**, Scatter plots showing inverse correlation of *BAP1* and *SLC7A11* expression in different cancer types. KIRC, $n = 606$ independent samples; KIRP, $n = 323$ independent samples; UVM, $n = 80$ independent samples; PCPG, $n = 187$ independent samples; BRCA, $n = 1{,}218$ independent samples. **c**,**g**,**i**, Box plots showing a comparison of *SLC7A11* or *BAP1* expression levels in normal tissues (N) and corresponding tumour (T) samples. KIRC, $n = 606$ independent samples; KIRP, $n = 323$ independent samples; normal kidney, $n = 28$ independent samples; PCPG, $n = 187$ independent samples; normal nerve, $n = 278$ independent samples; BRCA, $n = 1{,}218$ independent samples; normal breast, $n = 179$ independent samples. **d**, Kaplan–Meier plots of KIRC patients stratified by *SLC7A11* expression levels. **f**, Immunoblotting analyses of BAP1 and SLC7A11 protein levels in different cancer cell lines. The experiment was repeated twice, independently, with similar results. **h**, Bar graphs showing the frequencies of BAP1 genetic alterations in the indicated tumour types. Data are integrated from the cBioPortal (http://www.cbioportal.org/) using the indicated TCGA cancer datasets. The details of each cancer study can be dounf in the Data Availability statement. **j**,**k**, Kaplan–Meier plots of KIRP (**j**) and UVM (**k**) patients stratified by *SLC7A11* expression levels. **l**, Kaplan–Meier plots of UVM patients stratified by *BAP1* expression levels. **m**,**n**, Kaplan–Meier plots of KIRP (**m**) or UVM (**n**) patients stratified by unsupervised clustering on *BAP1* and *SLC7A11* expression. Group 1 has higher *BAP1* and lower *SLC7A11* expression, while Group 2 has lower *BAP1* and higher *SLC7A11* expression. Pearson's correlation (two-sided) analysis was used in **b** and **e**. Two-tailed unpaired Student's *t*-test was used in **c**,**g**,**i**. Log-rank Mantel–Cox test was used in **d**,**j**,**k**,**l**,**m**,**n**. Detailed statistical tests are described in the Methods. Scanned images of unprocessed blots are shown in Supplementary Fig. 7.

re-expression of *BAP1* WT, but not its C91A mutant, in UMRC6 cells decreased *SLC7A11* expression (Fig. 3a-c), suggesting that BAP1-mediated repression of *SLC7A11* expression requires BAP1's DUB activity. Similarly, *BAP1* re-expression in NCI-H226 cells, a *BAP1*-deficient mesothelioma cell line with high SLC7A11 expression (Fig. 2f), also repressed *SLC7A11* expression (Supplementary Fig. 2a,b). Conversely, *BAP1* deficiency by CRISPR technology increased SLC7A11 expression in several *BAP1*-proficient renal cancer cells with low SLC7A11 levels, including 786-O, Caki1 and ACHN cells (Fig. 3d,e and Supplementary 2c-f). Importantly, restoration of *BAP1* WT, but not its C91A mutant, in *BAP1* CRISPR knockout (KO) (sg*BAP1*) 786-O cells decreased *SLC7A11* expression

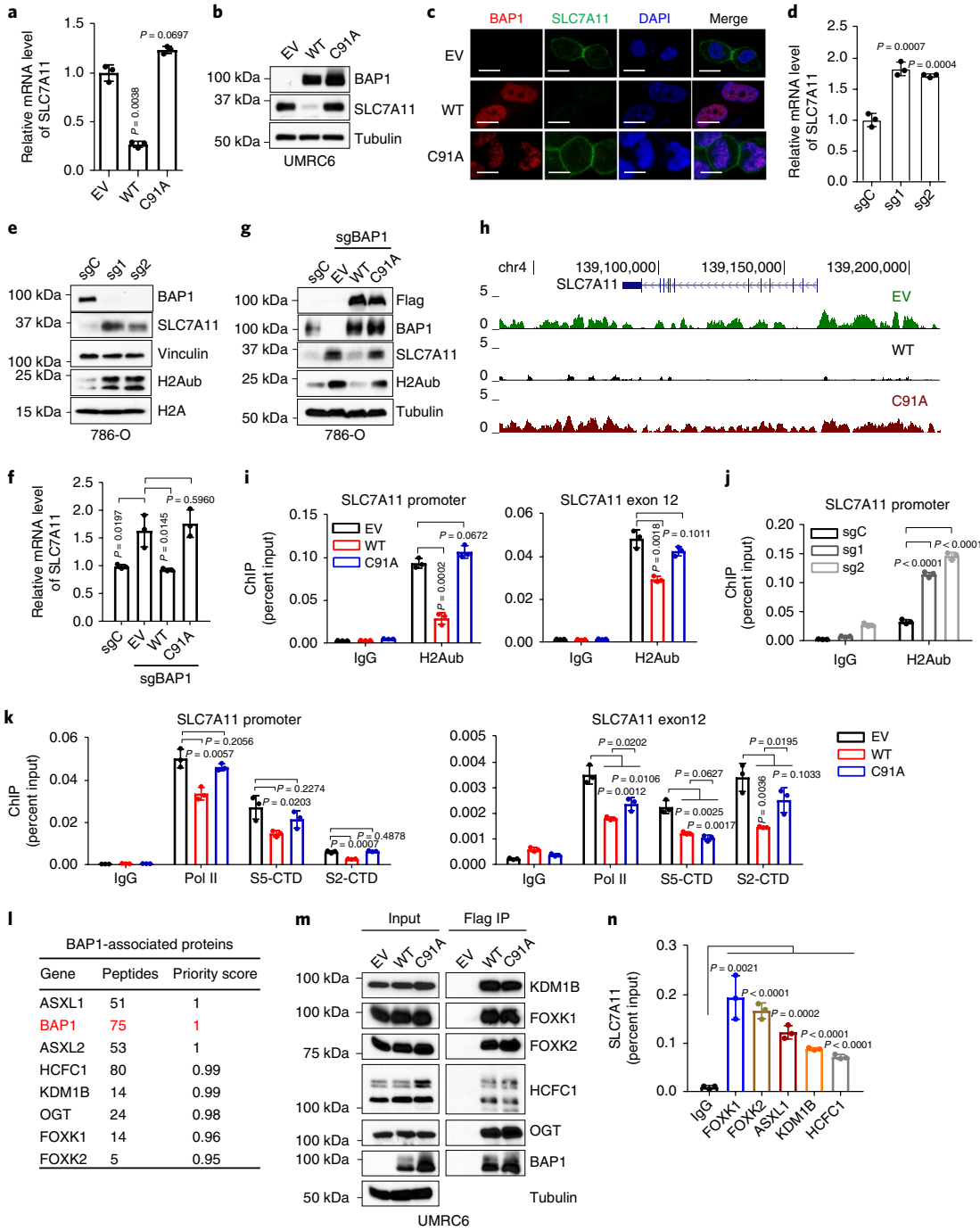

Fig. 3 | BAP1 suppresses *SLC7A11* expression and reduces H2Aub occupancy on the *SLC7A11* promoter. a,**b**, *SLC7A11* expression levels in the indicated UMRC6 cells were measured by RT–PCR (**a**) and western blotting (**b**). Error bars are mean ± s.d., $n = 3$ independent repeats (**a**). The experiment was repeated four times, independently, with similar results (**b**). **c**, BAP1 (red) and SLC7A11 (green) expression and localization in indicated cells were analysed by immunofluorescence. Cell nuclei were labelled by DAPI (blue) staining. Scale bar, 10 μm. The experiment was repeated twice independently with similar results. **d**,**e**, mRNA and protein levels of indicated genes in indicated 786-O cells were measured by RT–PCR (**d**) and western blotting (**e**). Error bars are mean ± s.d., $n = 3$ independent repeats (**d**). The experiment was repeated three times, independently, with similar results (**e**). **f**,**g**, mRNA and protein levels of indicated genes in indicated 786-O cells were measured by RT–PCR (**f**) and western blotting (**g**). Error bars are mean ± s.d., $n = 3$ independent repeats (**f**). The experiment was repeated twice, independently, with similar results (**g**). **h**, H2Aub ChIP–seq occupancy profiles at the *SLC7A11* loci in indicated UMRC6 cells. **i**, ChIP–qPCR confirming the lower H2Aub binding on the *SLC7A11* promoter and selected exon regions in *BAP1* WT cells than in EV or *BAP1* C91A cells. Error bars are mean ± s.d., $n = 3$ independent repeats. **j**, ChIP–qPCR showing the increased H2Aub binding on the *SLC7A11* promoter with *BAP1* deficiency in 786-O cells. Error bars are mean ± s.d., $n = 3$ independent repeats. **k**, ChIP–qPCR analysis of RNA polymerase II (Pol II), S5-CTD and S2-CTD binding on the *SLC7A11* promoter and selected exon regions. Error bars are mean ± s.d., $n = 3$ independent repeats. **l**, Lists of BAP1 binding proteins identified by mass spectrometry. **m**, Interactions between indicated proteins and BAP1 were verified by western blotting in the indicated cells. The experiment was repeated twice, independently, with similar results. **n**, Bar graph showing the binding of PR-DUB proteins on the *SLC7A11* promoter by ChIP–qPCR. Error bars are mean ± s.d., $n = 3$ independent repeats. All *P* values were calculated using two-tailed unpaired Student's *t*-test. Detailed statistical tests are described in the Methods. Scanned images of unprocessed blots are shown in Supplementary Fig. 7.

to a level similar to that in 786-O control cells (Fig. 3f,g). In addition, *Bap1* deletion in mouse embryonic fibroblasts (MEFs)[34] increased *SLC7A11* expression (Supplementary Fig. 2g). A luciferase assay with the *SLC7A11* promoter showed that overexpression of *BAP1* WT, but not its C91A mutant, decreased luciferase activity, whereas *BAP1* knockdown increased it, indicating that BAP1 regulates *SLC7A11* transcription (Supplementary Fig. 2h,i).

Previous studies showed that the tumour suppressor p53 represses *SLC7A11* expression[40,41]. Re-expression of *BAP1* in UMRC6 cells did not significantly affect p53 levels (Supplementary Fig. 2j). We then studied whether p53 plays a role in BAP1 regulation of *SLC7A11* expression. Consistent with previous findings in other cell lines[40], we confirmed that *p53* deletion via CRISPR technology increased SLC7A11 levels in UMRC6 cells (Supplementary Fig. 2k). However, restoring BAP1 in *p53*-deficient cells still inhibited *SLC7A11* expression (Supplementary Fig. 2l-n), and the fold change in *SLC7A11* expression by *BAP1* restoration in *p53*-deficient cells was similar to that in *p53*-proficient cells (Supplementary Fig. 2o), suggesting that BAP1 represses *SLC7A11* expression independent of p53.

Analysis of our H2Aub ChIP–seq data revealed that restoration of *BAP1* WT, but not *BAP1* C91A, markedly decreased H2Aub occupancy at both the promoter and gene body of *SLC7A11* (Fig. 3h), which was further confirmed by an H2Aub ChIP assay on the *SLC7A11* promoter and representative exons (Fig. 3i and Supplementary Fig. 2p). Conversely, we showed that *BAP1* deletion increased global H2Aub levels in 786-O, Caki1 and ACHN cells (Fig. 3e and Supplementary Fig. 2c,e) and promoted H2Aub binding on the *SLC7A11* promoter in 786-O cells (Fig. 3j). It has been shown that H2Aub regulates both transcription initiation and elongation[42], which are associated with different phosphorylation patterns of the heptad repeats of the C-terminal domain (CTD) of the largest subunit of RNA polymerase II: transcription initiation is associated with CTD serine 5 phosphorylation (S5-CTD), while transcription elongation is associated with CTD serine 2 phosphorylation (S2-CTD)[43]. We found that BAP1 decreased S5-CTD binding on the *SLC7A11* promoter and S2-CTD binding on exons of *SLC7A11* in a DUB-dependent manner (Fig. 3k and Supplementary Fig. 2q) (but BAP1 did not decrease the total protein levels of RNA polymerase II, S5-CTD or S2-CTD; Supplementary Fig. 2r). Our data thus suggest that BAP1-mediated H2Aub de-ubiquitination on *SLC7A11* correlates with inhibition of both transcription initiation and elongation.

BAP1 interacts with several transcriptional factors and chromatin-modifying factors, forming the PR–DUB complex[19,20]. Indeed, mass spectrometry analysis identified all known protein components of the PR–DUB complex as top-ranking BAP1-interacting proteins (Fig. 3l), and some of the interactions were further confirmed by co-immunoprecipitation analysis (Fig. 3m). It should be noted that BAP1 did not appear to affect the protein levels of other PR–DUB components (Supplementary Fig. 3a). It has been suggested that BAP1 is recruited to chromatin through the transcriptional factors and chromatin-modifying factors in the PR–DUB complex, such as FOXK1/2 and ASXL1/2[19]. A previous study generated ChIP–seq data sets for several components in the PR–DUB complex, including FOXK1, ASXL1 and O-GlcNAC (a readout for OGT)[44]. We therefore integrated these ChIP–seq data sets with our H2Aub data sets. These analyses identified around 3,000 genes that are co-occupied by FOXK1, ASXL1 and O-GlcNAC; among these, 1,140 genes also exhibit BAP1-dependent decrease in H2Aub occupancy (Supplementary Fig. 3b). Notably, analysis of these ChIP–seq data sets revealed striking bindings of ASXL1, FOXK1 and O-GlcNAC on the *SLC7A11* promoter (Supplementary Fig. 3c). The bindings of PR–DUB complex proteins on the *SLC7A11* promoter were further validated by ChIP assay (Fig. 3n). Knockdown of some PR–DUB components also affected *SLC7A11* expression (Supplementary Fig. 3d-m). Together, our data suggested a model that the BAP1-containing PR–DUB complex binds on the *SLC7A11* promoter, where BAP1 removes ubiquitin from H2Aub, and BAP1-dependent H2Aub reduction on *SLC7A11* is associated with BAP1-mediated *SLC7A11* repression.

BAP1 suppresses SLC7A11-mediated cystine uptake and promotes ferroptosis. SLC7A11 mediates the uptake of extracellular cystine, a major precursor for glutathione biosynthesis[12,14]. Glutathione is then utilized by GPX4 to detoxify lipid hydroperoxide and to protect cells from ferroptosis[15]. Consistently, we observed that re-expression of *BAP1* WT, but not its C91A mutant, in UMRC6 cells inhibited cystine uptake (Fig. 4a), decreased GSH levels (Fig. 4b) and increased erastin-induced lipid peroxidation (Fig. 4c). Erastin treatment potently induced *SLC7A11* expression without affecting *BAP1* expression (Supplementary Fig. 4a,b). In addition, erastin potently induced *SLC7A11* expression in *BAP1*-deficient cells (Supplementary Fig. 4c,d), suggesting that BAP1 represses the basal expression of *SLC7A11* and that erastin induces *SLC7A11* expression, probably through BAP1-independent mechanisms.

We next studied the potential role of BAP1 in ferroptosis. We showed that treatment with *tert*-butyl hydroperoxide (TBH), a ROS inducer[40], resulted in substantially more cell death in *BAP1* WT cells than in EV or *BAP1* C91A cells (Fig. 4d and Supplementary Fig. 4e). Importantly, TBH-induced cell death could be largely suppressed by the ferroptosis inhibitor ferrostatin or the iron chelator deferoxamine (DFO), but not by the apoptosis inhibitor Z-VAD-fmk or the necroptosis inhibitor necrostatin-1s (Fig. 4d). Similarly, *BAP1* WT, but not its C91A mutant, significantly potentiated erastin-induced cell death (Fig. 4e,f and Supplementary Fig. 4f), and erastin-induced cell death could be fully suppressed by ferrostatin or DFO, but not by Z-VAD-fmk or necrostatin-1s (Fig. 4g and Supplementary Fig. 4f). Erastin treatment did not induce poly (ADP-ribose) polymerase (PARP) cleavage (Fig. 4g), confirming that erastin did not induce apoptosis. Cystine depletion also induces ferroptosis[45]. We observed that expression of *BAP1* WT, but not the *BAP1* C91A mutant, sensitized UMRC6 cells to cystine-depletion-induced cell death, which could be fully suppressed by ferrostatin (Fig. 4h,i). Re-expression of *BAP1* in NCI-H226 cells, another *BAP1*-deficient cell line, similarly potentiated TBH- or erastin-induced ferroptosis (Supplementary Fig. 4h,i). Conversely, *BAP1* deficiency in 786-O, Caki1 and ACHN cells (Fig. 4j,k and Supplementary Fig. 4j,k) and in MEFs (Fig. 4l-n and Supplementary Fig. 4l,m) rendered cells more resistant to erastin- or cystine-depletion-induced ferroptosis. Importantly, re-expression of *BAP1* WT, but not its C91A mutant, in *BAP1* KO 786-O cells restored ferroptosis sensitivity (Fig. 4o). Finally, analysis of ferroptosis sensitivity in the panel of cell lines (Fig. 2f) revealed that all three BAP1-low/SLC7A11-high cell lines were resistant to erastin-induced ferroptosis, whereas five of seven BAP1-high/SLC7A11-low cell lines were sensitive to erastin-induced ferroptosis (Supplementary Fig. 4n). Taken together, our results convincingly showed that BAP1 promotes ferroptosis in a DUB-dependent manner.

BAP1 regulates ferroptosis through SLC7A11. We next sought to determine whether BAP1 promotes ferroptosis by mediating repression of *SLC7A11* expression. Restoration of *SLC7A11* in UMRC6 *BAP1* cells normalized cystine uptake, lipid peroxidation accumulation, and erastin-, ROS- or cystine-depletion-induced ferroptosis to levels similar to those observed in UMRC6 EV cells (Fig. 5a-g). We also restored *SLC7A11* expression in NCI-H226 *BAP1* cells and made similar observations (Supplementary Fig. 5a-e). Conversely, *SLC7A11* knockdown in UMRC6 and NCI-H226 cells, two *BAP1*-deficient cancer cells that exhibited high *SLC7A11* expression and were resistant to ferroptosis (Fig. 2f and Supplementary Fig. 4n), sensitized the cells to erastin- or cystine-depletion-induced

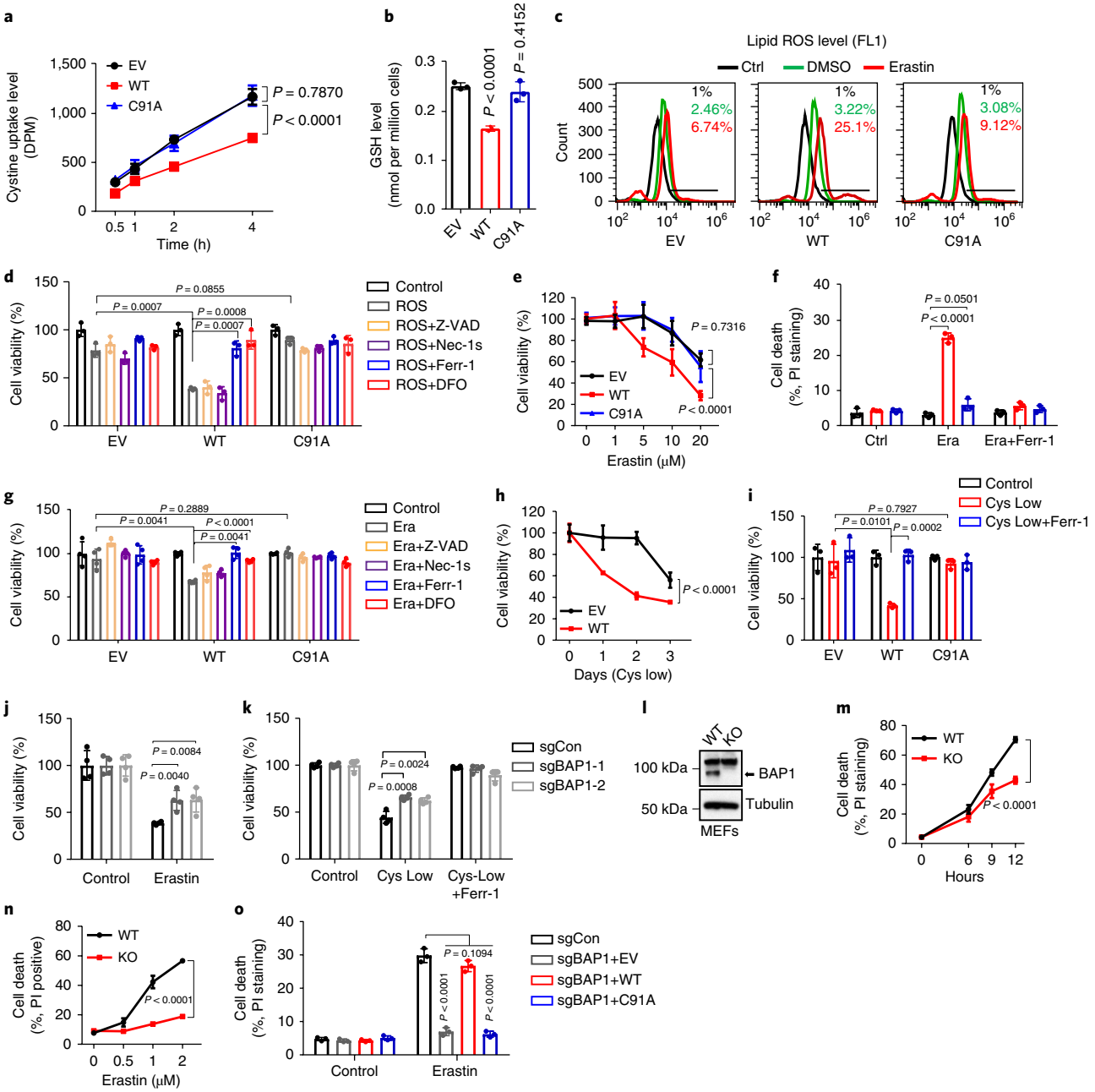

Fig. 4 | BAP1 suppresses SLC7A11-mediated cystine uptake and promotes ferroptosis. a, Cystine uptake levels measured in indicated cells. **b**, Bar graph showing intracellular GSH levels in indicated cells. **c**, Lipid peroxidation was assessed by flow cytometry after C11-BODIPY staining in indicated cells. The experiment was repeated three times, independently, with similar results. **d**,**g**, Bar graphs showing cell viability in indicated cells treated with ROS (100 μM TBH) (**d**) or 20 μM erastin (Era) (**g**) combined with 5 μM Z-VAD-fmk (Z-VAD), 2 μM Necrostatin-1s (Nec-1s), 2 μM ferrostatin-1 (Ferr-1) or 100 μM deferoxamine (DFO). **e**, Cell viability in indicated cells, measured after treatment with different concentrations of erastin for 30 h. **f**, Cell death measured in indicated cells after treatment with Ferr-1 (2 μM) and erastin (20 μM) for 24 h. **h**, Cell viability of indicated cells measured on culturing in cystine-low (2 μM cystine) medium for the indicated durations. **i**, Cell viability of indicated cells, measured after culturing in cystine-low medium + Ferr-1 (2 μM) for 48 h. **j**,**k**, Cell viability measured in *BAP1* KO 786-O cells treated with erastin (10 μM) for 24 h (**j**) or cultured in cystine-low medium + Ferr-1 (2 μM) for 24 h (**k**). **l**, Western blotting analysis of BAP1 expression in *Bap1* WT and KO MEFs. The experiment was repeated twice, independently, with similar results. **m**,**n**, Erastin-induced cell death in *Bap1* WT and KO MEFs at different time points (2 μM) (**m**) or at different concentrations after 8 h of treatment (**n**). **o**, Cell death measured in *BAP1* KO 786-O cells restored with BAP1 WT or C91A mutant and treated with erastin (10 μM) for 24 h. Error bars are mean ± s.d., $n = 3$ (**a**,**b**,**d**,**f**,**h**,**i**,**m**,**n**) or 4 (**e**,**g**,**j**,**k**) independent repeats. Two-way ANOVA analysis was performed in **a**,**e**,**h**,**m**,**n**. Two-tailed unpaired Student's *t*-test was performed in **b**,**d**,**f**,**g**,**i**,**j**,**k**,**o**. Detailed statistical tests are described in the Methods. Scanned images of unprocessed blots are provided in Supplementary Fig. 7.

ferroptosis (Fig. 5h-k and Supplementary Fig. 5f-i). Finally, *SLC7A11* knockdown in sg*BAP1* 786-O cells (which exhibited increased *SLC7A11* expression) also re-sensitized the cells to ferroptosis (Fig. 5l-n). Collectively, our data strongly suggest that BAP1 promotes ferroptosis mainly through BAP1-mediated repression of *SLC7A11* expression.

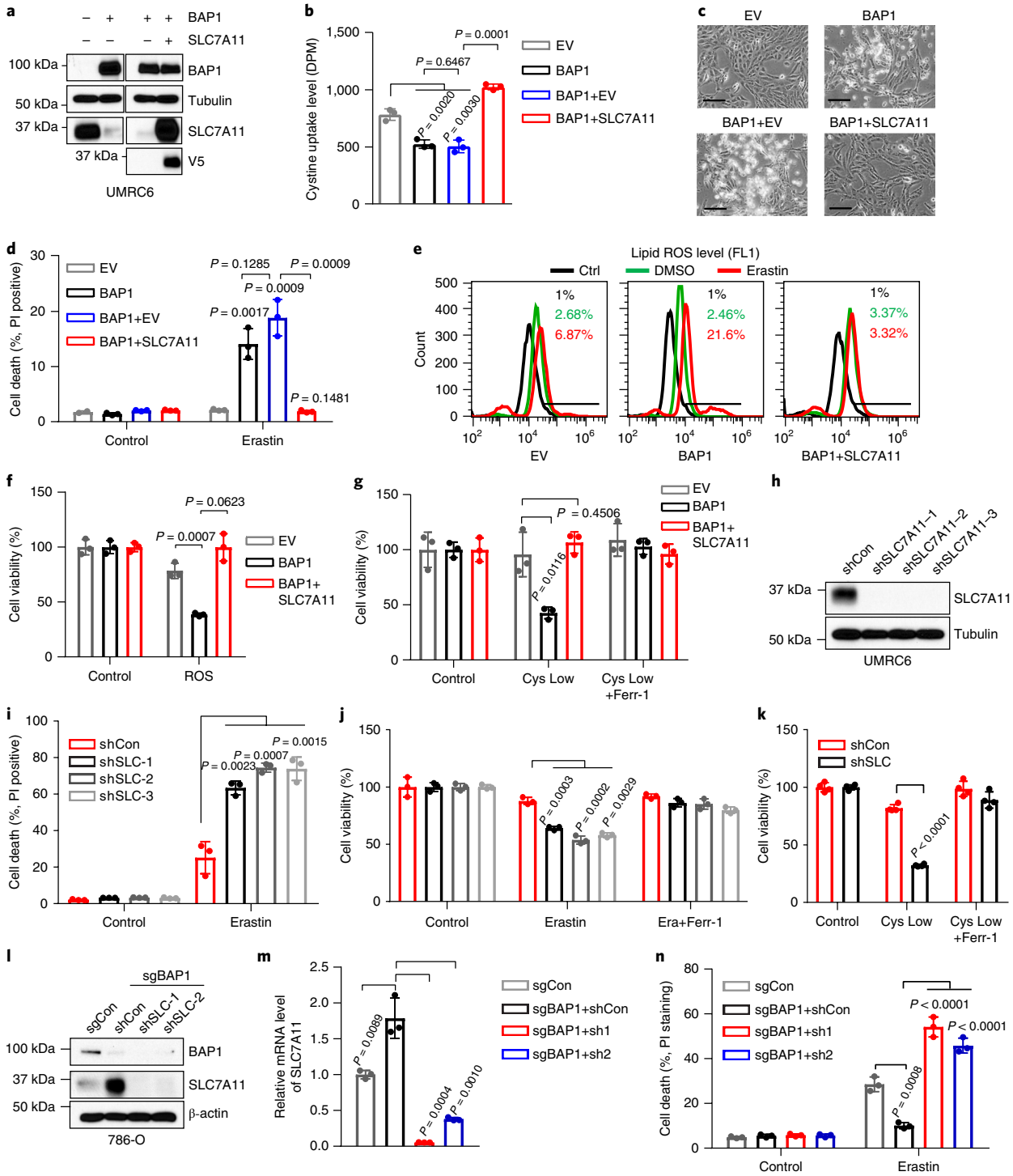

Fig. 5 | BAP1 promotes ferroptosis through SLC7A11. a, Western blotting analysis of BAP1 and SLC7A11 in the indicated cell lines. The experiment was repeated twice, independently, with similar results. **b**, Cystine uptake levels at 2 h were measured in the indicated cells. **c**, Representative phase-contrast images of the indicated cells treated with 20 μM erastin for 24 h. Scale bars, 100 μm. **d**, Bar graph showing cell death in the indicated cell lines following erastin treatment. **e**, Lipid peroxidation in the indicated cells after treatment with 10 μM erastin for 24 h, assessed by flow cytometry after C11-BODIPY staining. **f**, Bar graph showing cell death in the indicated cells induced by ROS (100 μM TBH, 16 h). **g**, Bar graph showing viability of the indicated cells cultured in cystine-low (2 μM) medium for 2 days with or without 2 μM ferrostatin-1 (Ferr-1). **h**, Western blotting analysis of SLC7A11 expression in *SLC7A11*-knockdown cell lines. The experiment was repeated twice, independently, with similar results. **i**, Bar graph showing cell death of the indicated cells following 20 μM erastin treatment for 30 h. **j**,**k**, Bar graphs showing viability of the indicated cells treated with erastin (10 μM) with or without 2 μM Ferr-1 for 30 h (**j**), or cultured in cystine-low medium with or without 2 μM Ferr-1 for 2 days (**k**). **l**,**m**, Western blotting (**l**) and RT–PCR (**m**) analyses of SLC7A11 in *BAP1* KO 786-O cell lines with *SLC7A11*-knockdown. The experiment was repeated twice, independently, with similar results (**l**). **n**, Bar graph showing cell death in the indicated cell lines after 10 μM erastin treatment for 24 h. Error bars are mean ± s.d., $n = 3$ (**b**,**d**,**f**,**g**,**i**,**j**,**m**,**n**) or 4 (**k**) independent repeats. All *P* values were calculated using two-tailed unpaired Student's *t*-test. Detailed statistical tests are described in the Methods. Scanned images of unprocessed blots are shown in Supplementary Fig. 7.

BAP1 inhibits tumour development partly through SLC7A11 and ferroptosis. We also studied the role of BAP1 regulation of *SLC7A11* in BAP1-mediated tumour suppression. *BAP1* re-expression in UMRC6 cells markedly inhibited anchorage-independent growth in a DUB-dependent manner (Fig. 6a). *SLC7A11* knockdown in UMRC6 cells significantly inhibited anchorage-independent growth (Fig. 6b), and importantly, restoration of *SLC7A11* in UMRC6 *BAP1* WT cells partially restored anchorage-independent growth compared with UMRC6 EV cells (Fig. 6c). It should be noted that *BAP1* re-expression or *SLC7A11* knockdown affected cell proliferation marginally (Fig. 6d,e). Consistently, we showed that *BAP1* re-expression in a *BAP1*-deficient background markedly inhibited xenograft tumour development and that restoration of *SLC7A11* in *BAP1*-expressing cells partially restored tumour development (Fig. 6f), while *SLC7A11* knockdown in a *BAP1*-deficient background inhibited xenograft tumour development (Fig. 6g,h). In addition, *BAP1* deletion in a *BAP1*-proficient background markedly increased xenograft tumour development, and restoration of *BAP1* WT, but not *BAP1* C91A mutant, repressed tumour development (Fig. 6i). Taken together, our data suggest that BAP1 suppresses tumour development in a DUB-dependent manner and at least partly through SLC7A11.

Next, we studied the potential relevance of ferroptosis in BAP1-mediated tumour suppression. Electron microscopy (EM) analysis revealed that many tumour cells from xenograft tumours with *BAP1* re-expression contained shrunken mitochondria with increased membrane density, a morphologic feature of ferroptosis[7]. In contrast, we never observed such cells in EV tumour samples (Fig. 6j). Because ferroptosis is characterized by overproduction of lipid peroxidation, we conducted 4-hydroxy-2-noneal (4HNE) immunohistochemistry (IHC) analysis to characterize lipid peroxidation levels[46] in EV and *BAP1*-re-expressing tumour samples. These studies revealed increased 4HNE staining in tumour cells, but not the surrounding lymphocytes, from *BAP1*-re-expressing tumours compared with cells from EV tumours (Fig. 6k,l). Finally, we showed that treatment with the ferroptosis inhibitor liproxstatin-1[16], while it did not affect EV tumour development, partially restored tumour development in *BAP1*-re-expressing tumours (Fig. 6m). Together, our data suggest that BAP1 promotes ferroptosis in vivo and that ferroptosis is at least partly responsible for BAP1's tumour suppression function in vivo.

Cancer-associated *BAP1* mutations are defective in regulating *SLC7A11* and ferroptosis. Many *BAP1* mutations have been identified in human cancers. A survey of cancer genomics data sets from the cBioPortal for Cancer Genomics[47,48] as of September 2017 identified about 500 somatic mutations in *BAP1*, including 211 nonsense (truncating) mutations and 283 missense mutations (Supplementary Fig. 6a). Importantly, KIRC patients with *BAP1* mutations had poor clinical outcomes (Supplementary Fig. 6b). To study the effect of cancer-associated *BAP1* missense mutations on ferroptosis and tumour suppression, we first utilized the Mutation Assessor from cBioPortal (http://mutationassessor.org/r2/) to predict and rank the functional impact scores of all missense mutations identified in *BAP1*. These analyses identified eight BAP1 mutations with the highest functional impact scores (Supplementary Table 3). Notably, all eight mutations are located within the UCH domain, which mediates the DUB activity of BAP1 (Fig. 7a). In fact, one mutation, C91G, is equivalent to C91A, which was used as the DUB-inactive mutant in our study. Thus, the mutation analyses strongly suggested an important role for BAP1 DUB function in human cancer. We then expressed each of these cancer-associated BAP1 mutants, as well as BAP1 WT and the C91A mutant, in UMRC6 cells. Remarkably, all BAP1 mutants, except G109V, behaved as loss-of-function mutants and were incapable of repressing *SLC7A11* expression (Fig. 7b,c) or promoting erastin- or cystine-depletion-induced ferroptosis (Fig. 7d,e and Supplementary Fig. 6c). We further showed that, while these mutants only affected cell proliferation moderately at most (Supplementary Fig. 6d,e), all mutants except G109V at least partially lost their abilities to inhibit anchorage-independent growth (Fig. 7f).

These BAP1 mutants did not significantly affect BAP1's interaction with other components of the PR–DUB complex (Supplementary Fig. 6f). Notably, we observed that all BAP1 mutants except G109V were incapable of downregulating H2Aub (Fig. 7b), suggesting that these BAP1 mutants are at least partially DUB-inactive toward H2Aub. Overall, we observed strong correlations of these cancer-associated BAP1 mutants in terms of their effects on H2Aub levels, *SLC7A11* expression, ferroptosis sensitivity and anchorage-independent growth. Collectively, our results provided direct evidence to link BAP1's functions in regulating H2Aub, *SLC7A11* expression and ferroptosis to its tumour suppression function in human cancer, and further suggested that BAP1's DUB function of removing H2Aub is involved in its regulation of *SLC7A11* expression, ferroptosis and tumour suppression.

Discussion

Tumour cells require an appropriate supply of amino acids, including cystine, to survive, grow and proliferate. Cystine plays important roles in maintaining redox balance and promoting cell survival in tumour cells, and an insufficient cystine supply induces metabolic stress and provokes ferroptotic cell death in tumour cells[7]. Tumour cells engage different strategies to ensure an adequate supply of cystine from the tumour microenvironment. In some tumour cells with low expression of cystine transporter *SLC7A11*, such as chronic lymphocytic leukaemia cells, stromal cells surrounding the tumour take up cystine, convert cystine to cysteine, and release cysteine into the tumour microenvironment; cysteine reuptake into tumour cells then promotes survival[49]. In contrast, other types of tumour cell upregulate the expression of *SLC7A11* and maintain high cystine uptake, although the underlying mechanisms by which tumour cells maintain high *SLC7A11* expression remain incompletely understood. Our study revealed an important epigenetic mechanism linking SLC7A11 regulation of ferroptosis to tumour biology. Specifically, our study suggests a model in which the tumour suppressor BAP1 normally functions to repress the expression of *SLC7A11* at least partly by deubiquitinating H2Aub on *SLC7A11*, thereby inhibiting cystine uptake into cells and rendering them more sensitive to ferroptosis. *BAP1* inactivation by either mutation or expression downregulation de-represses *SLC7A11* expression in tumour cells, resulting in increased cystine uptake and GSH synthesis, enhanced resistance to ferroptotic cell death, and promotion of tumour development. Notably, our integrated transcriptomic/epigenomic/cancer genomic analyses identified SLC7A11 as a BAP1 target with the most relevance to BAP1-mediated tumour suppression in human cancers, suggesting that the model described above is likely to be an important mechanism mediating BAP1's tumour suppression function, although we do not rule out the possibility that other BAP1 targets, either transcriptional or non-transcriptional targets[50], may also play roles in BAP1-mediated tumour suppression.

Our study suggested that BAP1 represses *SLC7A11* expression through BAP1-mediated H2Aub deubiquitination on *SLC7A11*. Other studies in mammalian cells have also shown that BAP1 represses the expression of some target genes with BAP1-dependent deubiquitination of H2Aub on the corresponding gene promoters[21,51]. However, the underlying mechanisms by which BAP1-mediated H2Aub deubiquitination represses target genes remain poorly understood, given that H2Aub generally correlates with gene repression[29]. One model proposes that both H2A ubiquitination and deubiquitination need to occur in a dynamically regulated manner to maintain the repression of some target genes[52]. Similarly, it has been proposed that the cycling of H2B ubiquitination and

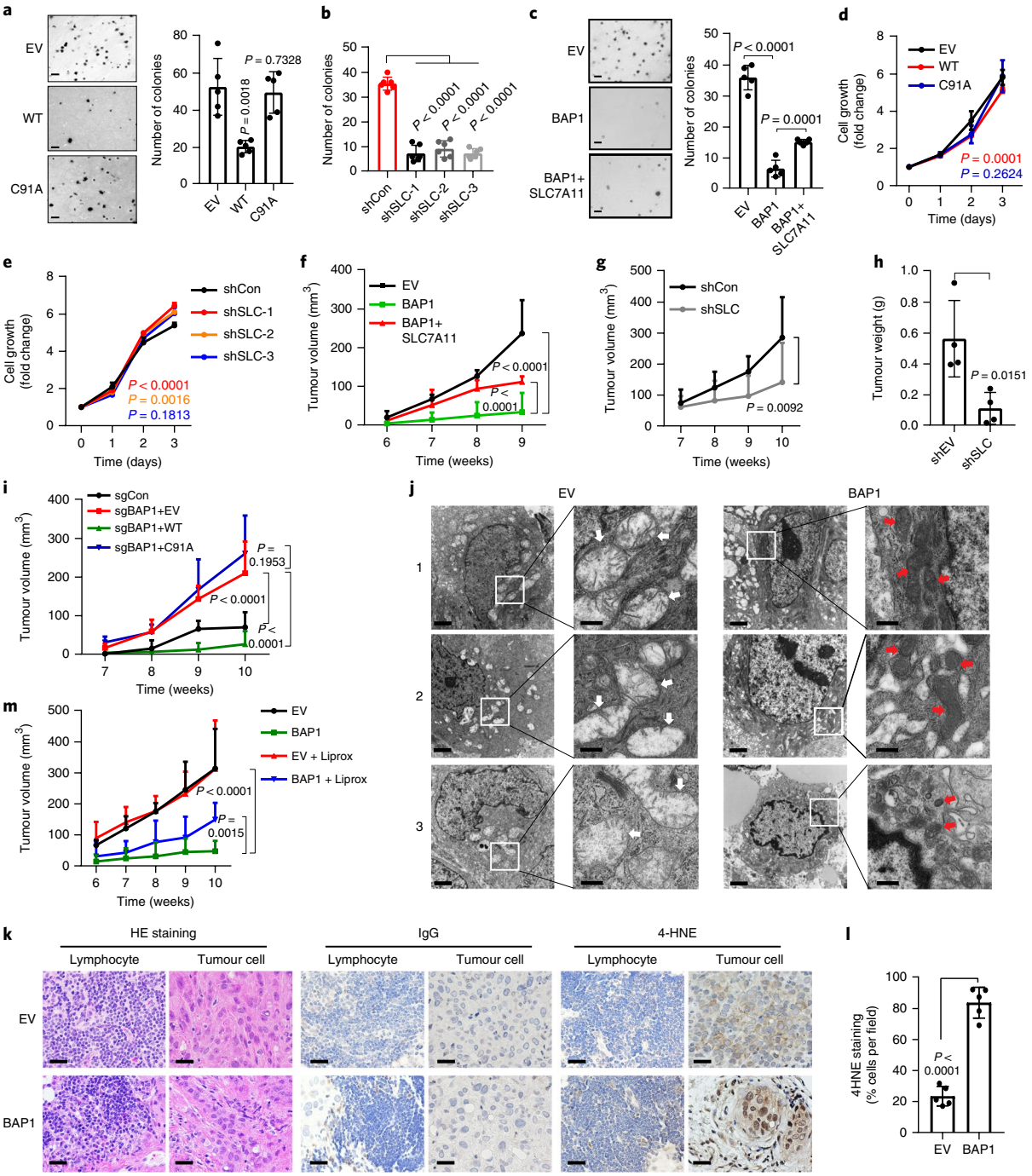

Fig. 6 | BAP1 inhibits tumour development partly through SLC7A11 and ferroptosis. a–c, Representative images showing colonies of the indicated cell lines on soft agar. Scale bars, 500 μm. Bar graph showing the relative number of colonies formed by the indicated cells in the soft agar assay. Error bars are mean ± s.d., $n = 5$ (**a**,**c**) or 6 (**b**) independent repeats. *P* values calculated using two-tailed unpaired Student's *t*-test. **d**,**e**, Cell growth assays of UMRC6 cells with indicated genotypes. Error bars are mean ± s.d., $n = 3$ (**e**) or 4 (**d**) independent repeats. *P* values determined using two-way ANOVA analysis. **f**,**g**, Volumes of xenograft tumours with the indicated genotypes at different time points (weeks) after tumour cell injection. Error bars are mean ± s.d., $n = 5$ independent repeats. *P* values determined using two-way ANOVA analysis. **h**, Bar graph showing the weight of tumour xenografts from the indicted genotypes. Error bars are mean ± s.d., $n = 5$ independent repeats. *P* values calculated using two-tailed unpaired Student's *t*-test. **i**, Tumour volumes of xenograft tumours from 786-O cell lines with indicated genotypes at different weeks. Error bars are mean ± s.d., $n = 5$ (sgCon and sgBAP1 + EV) or 8 (sgBAP1 + WT and BAP1 + C91A) independent repeats. *P* values determined using two-way ANOVA analysis. **j**, Tumour xenografts from EV and BAP1-restored cell lines subjected to transmission electron microscopy. White arrows, mitochondria with obvious cristae; red arrows, shrunken mitochondria. Scale bars: left, 2 μm; right, 500 nm. The experiment was repeated twice, independently, with similar results. **k**, Haematoxylin and eosin and immunohistochemical staining of tumour xenografts from the EV and BAP1-restored cell lines. Scale bars, 50 μm. The experiment was repeated twice, independently, with similar results. **l**, Percentage of 4HNE-positive stained cells per field. Error bars are mean ± s.d., $n = 5$ randomly selected high-power fields. *P* values calculated using two-tailed unpaired Student's *t*-test. **m**, Volumes of xenograft tumours with the indicated genotypes and treatments at different weeks. Error bars are mean ± s.d., $n = 5$ independent repeats. *P* values determined using two-way ANOVA analysis. Detailed statistical tests are described in the Methods.

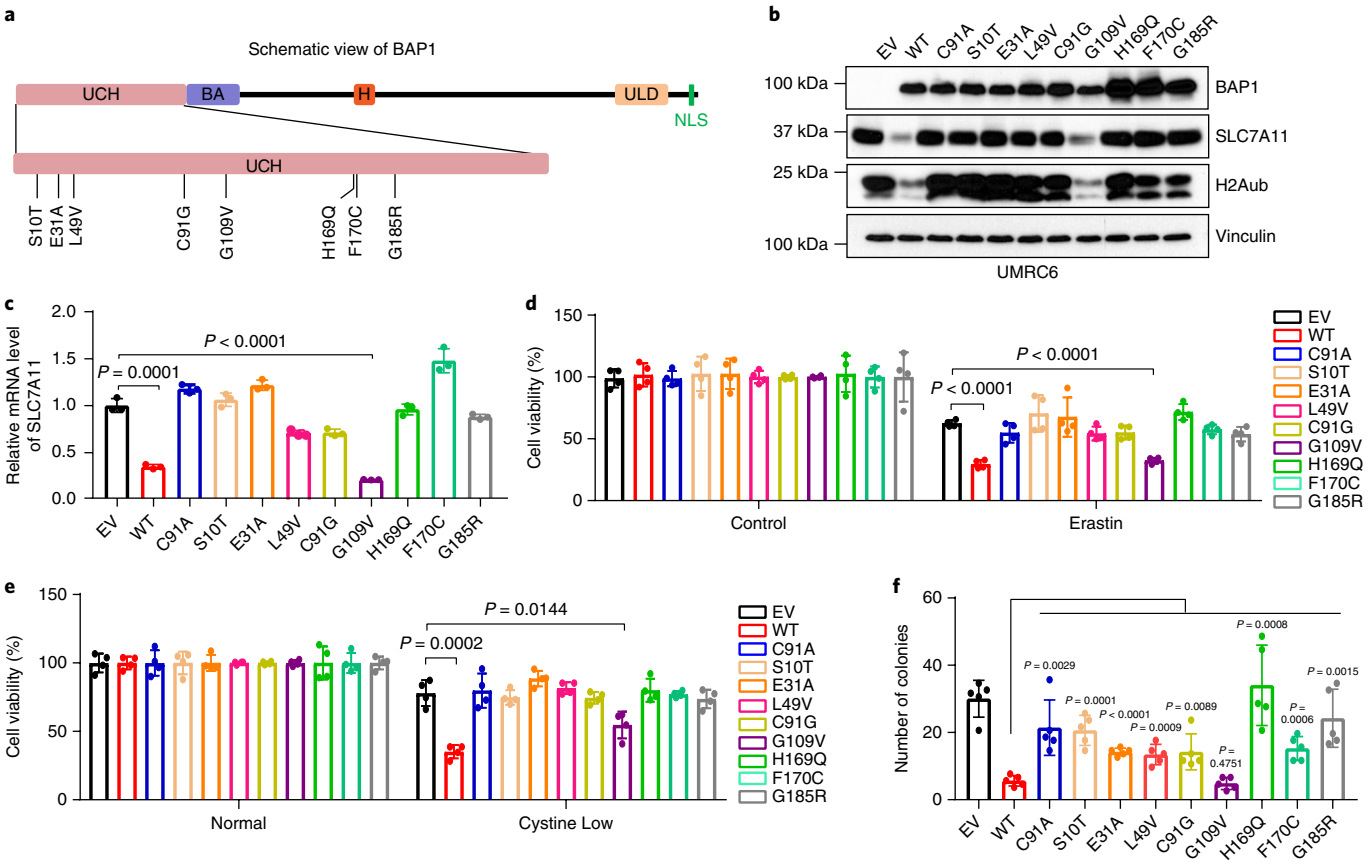

Fig. 7 | Cancer-associated *BAP1* mutations are defective in regulating *SLC7A11* and ferroptosis. a, Diagram showing BAP1 domain structure and mutated sites of cancer-associated *BAP1* mutations generated in this study. UCH, ubiquitin C-terminal hydrolases; BA, BRCA1-binding domain; H, HCF1-binding domain; ULD, UCH37-like domain; NLS, nuclear localization signal. **b**, Western blot analysis of UMRC6 cells with re-expression of cancer-associated BAP1 mutants and WT BAP1 as indicated. The experiment was repeated twice, independently, with similar results. **c**, Relative mRNA levels of *SLC7A11* in the indicated UMRC6 cells were determined by RT–PCR. Error bars are mean ± s.d., $n = 3$ independent repeats. *P* values calculated using two-tailed unpaired Student's *t*-test. **d**,**e**, Bar graphs showing the viability of the indicated cells treated with 20 μM erastin for 30 h (**e**) or cultured in cystine-low (2 μM) medium for 2 days (**e**). Error bars are mean ± s.d., $n = 4$ independent repeats. *P* values calculated using two-tailed unpaired Student's t-test. **f**, Bar graph showing the relative number of colonies of the indicated cells in the soft agar assay. Error bars are mean ± s.d., $n = 5$ independent repeats. *P* values calculated using two-tailed unpaired Student's *t*-test. Detailed statistical tests are described in the Methods. Scanned images of unprocessed blots are shown in Supplementary Fig. 7.

deubiquitination is critical for transcriptional activation[53]. In line with this model, in *Drosophila*, the repression of polycomb target genes requires not only polycomb repressive complex 1 (PRC1)-mediated H2A ubiquitination, but also BAP1-mediated H2A deubiquitination, suggesting that an appropriate balance between H2A ubiquitination and deubiquitination, rather than H2A ubiquitination per se, is important for the maintenance of polycomb target gene repression[26]. Thus, it is possible that BAP1, by removing ubiquitin from H2Aub on some target genes, such as *SLC7A11*, facilitates the dynamic cycling of H2Aub, resulting in transcriptional repression of target genes. It will be interesting to test this hypothesis in future studies.

In cell line studies, ferroptosis can be specifically induced by cystine depletion or treatment with drugs such as erastin. It can be characterized by EM analysis and cell death inhibitor rescue experiments (that is, ferroptotic cell death can be prevented by ferroptosis inhibitors but not by inhibitors of other forms of cell death). Currently, our ability to study the clinical relevance of ferroptosis in cancer biology is hindered by a lack of established assays for characterizing ferroptosis in tissue and tumour samples equivalent to cleaved caspase-3 IHC staining for apoptosis. To our knowledge ferroptosis has not previously been identified in tumour samples in vivo. In our study, we conducted EM analysis, the gold standard assay for characterizing cell death, on tumour samples and provided definitive evidence of ferroptosis in tumours with *BAP1* re-expression. Our work thus motivates further studies to develop assays that can be routinely used for characterizing ferroptosis in tissue and tumour samples.

Methods

Methods, including statements of data availability and any associated accession codes and references, are available at https://doi.org/10.1038/s41556-018-0178-0.

Received: 12 October 2017; Accepted: 26 July 2018;
Published online: 10 September 2018

References

1. Pavlova, N. N. & Thompson, C. B. The emerging hallmarks of cancer metabolism. *Cell Metab.* **23**, 27–47 (2016).
2. DeBerardinis, R. J. & Chandel, N. S. Fundamentals of cancer metabolism. *Sci. Adv.* **2**, e1600200 (2016).
3. Green, D. R., Galluzzi, L. & Kroemer, G. Cell biology. Metabolic control of cell death. *Science* **345**, 1250256 (2014).

4. Boroughs, L. K. & DeBerardinis, R. J. Metabolic pathways promoting cancer cell survival and growth. *Nat. Cell. Biol.* **17**, 351–359 (2015).
5. Jones, R. G. & Thompson, C. B. Tumor suppressors and cell metabolism: a recipe for cancer growth. *Genes Dev.* **23**, 537–548 (2009).
6. Hanahan, D. & Weinberg, R. A. Hallmarks of cancer: the next generation. *Cell* **144**, 646–674 (2011).
7. Dixon, S. J. et al. Ferroptosis: an iron-dependent form of nonapoptotic cell death. *Cell* **149**, 1060–1072 (2012).
8. Xie, Y. et al. Ferroptosis: process and function. *Cell Death Differ.* **23**, 369–379 (2016).
9. Cao, J. Y. & Dixon, S. J. Mechanisms of ferroptosis. *Cell Mol. Life Sci.* **73**, 2195–2209 (2016).
10. Yang, W. S. & Stockwell, B. R. Ferroptosis: death by lipid peroxidation. *Trends Cell Biol.* **26**, 165–176 (2016).
11. Stockwell, B. R. et al. Ferroptosis: a regulated cell death nexus linking metabolism, redox biology, and disease. *Cell* **171**, 273–285 (2017).
12. Lim, J. C. & Donaldson, P. J. Focus on molecules: the cystine/glutamate exchanger (System x(c)(-)). *Exp. Eye Res.* **92**, 162–163 (2011).
13. Conrad, M. & Sato, H. The oxidative stress-inducible cystine/glutamate antiporter, System x(c)(-): cystine supplier and beyond. *Amino Acids* **42**, 231–246 (2012).
14. Koppula, P., Zhang, Y., Zhuang, L. & Gan, B. Amino acid transporter SLC7A11/xCT at the crossroads of regulating redox homeostasis and nutrient dependency of cancer. *Cancer Commun.* **38**, 12 (2018).
15. Yang, W. S. et al. Regulation of ferroptotic cancer cell death by GPX4. *Cell* **156**, 317–331 (2014).
16. Friedmann Angeli, J. P. et al. Inactivation of the ferroptosis regulator Gpx4 triggers acute renal failure in mice. *Nat. Cell. Biol.* **16**, 1180–1191 (2014).
17. Igney, F. H. & Krammer, P. H. Death and anti-death: tumour resistance to apoptosis. *Nat. Rev. Cancer* **2**, 277–288 (2002).
18. Green, D. R. & Evan, G. I. A matter of life and death. *Cancer Cell* **1**, 19–30 (2002).
19. Carbone, M. et al. BAP1 and cancer. *Nat. Rev. Cancer* **13**, 153–159 (2013).
20. Dey, A. et al. Loss of the tumor suppressor BAP1 causes myeloid transformation. *Science* **337**, 1541–1546 (2012).
21. Ji, Z. et al. The forkhead transcription factor FOXK2 acts as a chromatin targeting factor for the BAP1-containing histone deubiquitinase complex. *Nucleic Acids Res.* **42**, 6232–6242 (2014).
22. Baymaz, H. I. et al. MBD5 and MBD6 interact with the human PR–DUB complex through their methyl-CpG-binding domain. *Proteomics* **14**, 2179–2189 (2014).
23. Yu, H. et al. The ubiquitin carboxyl hydrolase BAP1 forms a ternary complex with YY1 and HCF-1 and is a critical regulator of gene expression. *Mol. Cell. Biol.* **30**, 5071–5085 (2010).
24. Misaghi, S. et al. Association of C-terminal ubiquitin hydrolase BRCA1-associated protein 1 with cell cycle regulator host cell factor 1. *Mol. Cell. Biol.* **29**, 2181–2192 (2009).
25. Machida, Y. J., Machida, Y., Vashisht, A. A., Wohlschlegel, J. A. & Dutta, A. The deubiquitinating enzyme BAP1 regulates cell growth via interaction with HCF-1. *J. Biol. Chem.* **284**, 34179–34188 (2009).
26. Scheuermann, J. C. et al. Histone H2A deubiquitinase activity of the polycomb repressive complex PR-DUB. *Nature* **465**, 243–247 (2010).
27. Kallin, E. M. et al. Genome-wide uH2A localization analysis highlights Bmi1-dependent deposition of the mark at repressed genes. *PLoS Genet.* **5**, e1000506 (2009).
28. Weake, V. M. & Workman, J. L. Histone ubiquitination: triggering gene activity. *Mol. Cell* **29**, 653–663 (2008).
29. Wang, H. et al. Role of histone H2A ubiquitination in polycomb silencing. *Nature* **431**, 873–878 (2004).
30. Harbour, J. W. et al. Frequent mutation of BAP1 in metastasizing uveal melanomas. *Science* **330**, 1410–1413 (2010).
31. Pena-Llopis, S. et al. BAP1 loss defines a new class of renal cell carcinoma. *Nat. Genet.* **44**, 751–759 (2012).
32. Jiao, Y. et al. Exome sequencing identifies frequent inactivating mutations in BAP1, ARID1A and PBRM1 in intrahepatic cholangiocarcinomas. *Nat. Genet.* **45**, 1470–1473 (2013).
33. Bott, M. et al. The nuclear deubiquitinase BAP1 is commonly inactivated by somatic mutations and 3p21.1 losses in malignant pleural mesothelioma. *Nat. Genet.* **43**, 668–672 (2011).
34. Dai, F. et al. BAP1 inhibits the ER stress gene regulatory network and modulates metabolic stress response. *Proc. Natl Acad. Sci. USA* **114**, 3192–3197 (2017).
35. Cancer Genome Atlas Research Network Comprehensive molecular characterization of clear cell renal cell carcinoma. *Nature* **499**, 43–49 (2013).
36. Robertson, A. G. et al. Integrative analysis identifies four molecular and clinical subsets in uveal melanoma. *Cancer Cell* **32**, 204–220 (2017).
37. Fishbein, L. et al. Comprehensive molecular characterization of pheochromocytoma and paraganglioma. *Cancer Cell* **31**, 181–193 (2017).
38. Cancer Genome Atlas Research Network Comprehensive molecular characterization of papillary renal-cell carcinoma. *N. Engl. J. Med.* **374**, 135–145 (2016).
39. Cancer Genome Atlas Research Network Comprehensive molecular portraits of human breast tumours. *Nature* **490**, 61–70 (2012).
40. Jiang, L. et al. Ferroptosis as a p53-mediated activity during tumour suppression. *Nature* **520**, 57–62 (2015).
41. Wang, S. J., Ou, Y., Jiang, L. & Gu, W. Ferroptosis: a missing puzzle piece in the p53 blueprint? *Mol. Cell. Oncol.* **3**, e1046581 (2016).
42. Vissers, J. H., Nicassio, F., van Lohuizen, M., Di Fiore, P. P. & Citterio, E. The many faces of ubiquitinated histone H2A: insights from the DUBs. *Cell Divis.* **3**, 8 (2008).
43. Li, B., Carey, M. & Workman, J. L. The role of chromatin during transcription. *Cell* **128**, 707–719 (2007).
44. Hauri, S. et al. A high-density map for navigating the human polycomb complexome. *Cell Rep.* **17**, 583–595 (2016).
45. Gao, M., Monian, P., Quadri, N., Ramasamy, R. & Jiang, X. Glutaminolysis and transferrin regulate ferroptosis. *Mol. Cell* **59**, 298–308 (2015).
46. Young, O., Crotty, T., O'Connell, R., O'Sullivan, J. & Curran, A. J. Levels of oxidative damage and lipid peroxidation in thyroid neoplasia. *Head Neck* **32**, 750–756 (2010).
47. Gao, J. et al. Integrative analysis of complex cancer genomics and clinical profiles using the cBioPortal. *Sci. Signal* **6**, pl1 (2013).
48. Cerami, E. et al. The cBio cancer genomics portal: an open platform for exploring multidimensional cancer genomics data. *Cancer Discov.* **2**, 401–404 (2012).
49. Zhang, W. et al. Stromal control of cystine metabolism promotes cancer cell survival in chronic lymphocytic leukaemia. *Nat. Cell. Biol.* **14**, 276–286 (2012).
50. Bononi, A. et al. BAP1 regulates IP3R3-mediated Ca^{2+} flux to mitochondria suppressing cell transformation. *Nature* **546**, 549–553 (2017).
51. Okino, Y., Machida, Y., Frankland-Searby, S. & Machida, Y. J. BRCA1-associated protein 1 (BAP1) deubiquitinase antagonizes the ubiquitin-mediated activation of FoxK2 target genes. *J. Biol. Chem.* **290**, 1580–1591 (2015).
52. Schuettengruber, B. & Cavalli, G. The DUBle life of polycomb complexes. *Dev. Cell* **18**, 878–880 (2010).
53. Henry, K. W. et al. Transcriptional activation via sequential histone H2B ubiquitylation and deubiquitylation, mediated by SAGA-associated Ubp8. *Genes Dev.* **17**, 2648–2663 (2003).

Acknowledgements

The authors thank X. Shi for helpful discussion and suggestions and A. Ninetto from the Department of Scientific Publications at The University of Texas MD Anderson Cancer Center for manuscript editing. This research was supported by the Andrew Sabin Family Fellow Award, the Sister Institution Network Fund, an Institutional Research Grant from The University of Texas MD Anderson Cancer Center, Anna Fuller Fund (to B.G.) and grants from the National Institutes of Health (R01CA181196 to B.G.; R01HG007538 and R01CA193466 to W.L.; R01CA172724 to P.H.). B.G. is an Ellison Medical Foundation New Scholar and an Andrew Sabin Family Fellow. Y.Z. and P.K. are Scholars at the Center for Cancer Epigenetics at The University of Texas MD Anderson Cancer Center. P.K. is supported by a CPRIT Research Training Grant (RP170067). This research was also supported by a National Institutes of Health Cancer Center Support Grant P30CA016672 to The University of Texas MD Anderson Cancer Center.

Author contributions

Y.Z. performed most of the experiments shown in Figs. 3–7 with assistance from X. Liu, P.K., K.S., H.L., L.Z. and Z.X. J.S. conducted all the computational analyses shown in Figs. 1 and 2. F.L. and G.C. helped with cystine uptake experiments. W.Y. helped with the 4HNE IHC analysis. Z.G. conducted tandem affinity purification to identify BAP1-associated proteins. X.Li analysed BAP1-associated proteins. B.G. and W.L. supervised the study. Y.Z. and B.G. designed the experiments and wrote the manuscript. J.C., M.H. and P.H. helped with discussion and interpretation of results. All authors commented on the manuscript.

Competing interests

The authors declare no competing interests.

Additional information

Supplementary information is available for this paper at https://doi.org/10.1038/s41556-018-0178-0.

Reprints and permissions information is available at www.nature.com/reprints.

Correspondence and requests for materials should be addressed to W.L. or B.G.

Publisher's note: Springer Nature remains neutral with regard to jurisdictional claims in published maps and institutional affiliations.

Methods

Cell culture studies. Cell line sources are detailed in the Reporting Summary. All cell lines were free of mycoplasma contamination (tested by the vendor). *Bap1* WT and KO MEFs were described in our previous publication[34]. For cystine deprivation experiments, cells were cultured in DMEM with different concentrations of cystine + 10% (vol/vol) dialysed FBS. The use of dialysed FBS is described in our previous publication[54]. To generate stable cell lines overexpressing Flag-BAP1 or mutant BAP1, HEK293T cells were transfected with either pLVX-Flag-BAP1 or mutant BAP1 constructs, together with psPAX.2 and pMD2.G third-generation lentiviral packaging systems using Lipofectamine 3000 reagent (ThermoFisher Scientific), according to the manufacturer's instructions. After 48 h, lentivirus particles in the medium were collected and filtered, then the target cell lines were infected. At 24 h post infection, an appropriate selection antibiotic was added to obtain stable cell lines with successful transduction. To generate CRISPR KO cells, the sgRNAs were cloned into the CRISPR-V2 vector (Addgene, #52961), and lentiviral infection was conducted as described above. After 72 h, single antibiotic selection-positive cells were sorted and plated into 96-well plates. Surviving KO clones were screened by immunoblotting with corresponding antibodies. To generate shRNA-knockdown cell lines, lentiviral transduction with shRNA vectors was conducted as described above. At 72 h later, following antibiotic selection, expression levels of target genes were determined by immunoblotting with corresponding antibodies.

Constructs and reagents. *SLC7A11* shRNAs and *SLC7A11* cDNA-containing expression vectors are described in our previous publication[55]. Human *BAP1* cDNA was cloned into the lentivirus vector pLVX-Puro with N-terminal FLAG tag. A series of mutant pLVX-Flag-BAP1 constructs were generated by PCR mutagenesis using a QuikChange II XL Site-Directed Mutagenesis Kit (Agilent) for amino acid substitutions according to the manufacturer's instructions. All constructs were confirmed by DNA sequencing. The sequences of primers used in PCR mutagenesis, gRNAs and shRNAs used in this study are listed in Supplementary Table 4. Erastin, ferrostatin-1 and TBH were obtained from Sigma (E7781, SML0583 and 458139). Z-VAD-fmk was obtained from R&D Systems (FMK001). Necrostatin-1s was obtained from BioVision (2263). Staurosporine was obtained from LC Laboratories (S-9300). All drugs were dissolved according to the manufacturers' instructions.

Cell death, viability and proliferation assays. To measure cell death, cells were seeded in a 12-well plate 1 day before treatment. After treatment with appropriate drugs, cells were trypsinized and collected in a 1.5 ml tube, washed once with PBS, and stained with 2 μg ml^{-1} PI (Roche) in PBS. Dead cells (PI-positive cells) were analysed using a BD Accuri C6 flow cytometer (BD Biosciences)[56,57]. To measure cell viability, 5,000 cells per well were seeded in a 96-well plate 1 day before treatment. Following treatment with the appropriate drugs where indicated, each well was replaced with fresh medium containing Cell Counting Kit-8 (CCK8) reagent (Sigma). After incubation for 1 h at 37 °C, the plate was analysed using a FLUOstar Omega microplate reader (BMG Labtech), and absorbance of the wells was measured at 540 nm. To measure cell proliferation, 1,500 cells per well were seeded in a 96-well plate. At 24 h after seeding, cell viability was measured using CCK8 reagent as described above. This was considered day 0. Later, cell viability was analysed every 24 h, and absorbance was normalized to that measured on day 0. Cell growth was indicated by the fold change from day 0 to as long as day 4, and was graphed[58,59].

Lipid peroxidation assay. Lipid peroxidation levels were measured as previously described[15]. Briefly, cells were incubated in a 60 mm dish containing 5 μM BODIPY 581/591 C11 dye (Invitrogen, D3861). After incubation for 30 min at 37 °C, cells were washed with PBS and trypsinized, then stained with PI (propidium iodide) in PBS for 5 min. Cells were then subjected to flow cytometry analysis using an Accuri C6 flow cytometer. The FL1 channel signal in live cells was plotted as shown in the figures.

Cystine uptake assay. Assessment of cystine uptake was conducted using modifications of a previously described protocol[49]. Briefly, cells were seeded in a 12-well plate and incubated overnight. To measure cystine uptake, the medium was replaced with fresh DMEM (which contains 200 μM cystine) containing [^{14}C] cystine (PerkinElmer) (0.04 μCi), and cells were incubated for the indicated time periods. Uptake was terminated by rapidly rinsing cells twice with cold PBS, and lysed in 0.1 mM NaOH. Radioactivity (DPM) was measured using Tri-Carb Liquid Scintillation Analyzer (PerKinElmer, Model 4810TR) in the presence of quench curve. All experiments were carried out in triplicate.

GSH assay. GSH levels were detected using a GSH-Glo Glutathione Assay (Promega) following the manufacturer's instructions. Briefly, 6,000 cells per well were seeded in a 96-well plate 1 day before analysis. The culture medium from the wells was carefully removed, and 100 μl of prepared 1 × GSH-Glo Reagent was added, followed by incubation at room temperature for 30 min. Next, 100 μl of reconstituted Luciferin Detection Reagent was added to each well and mixed briefly on a plate shaker. After 20 min, luminescence was measured using a Gen5 Microplate reader (BIOTEK). A standard curve for GSH concentration was generated, and exact GSH concentrations in different cell lines were calculated based on a GSH standard curve according to the manufacturer's instructions.

Light microscopy and immunofluorescence microscopy. For light microscopy, cells cultured in six-well plates were treated with reagents as indicated. Phase contrast images were obtained using an EVOSfl (Advanced Microscopy Group) microscope equipped with a ×10 phase contrast objective. For trypan blue staining, cells were trypsinized and collected in a 1.5 ml tube. Cell pellets were washed once in PBS and then stained with trypan blue (Corning) for 5 min. A ×20 phase contrast objective was used to acquire photographs of stained dead cells. For immunofluorescence microscopy, cells were seeded on glass coverslips and washed with PBS, then fixed in 3.7% formaldehyde. After fixation, cells were washed with PBS and permeabilized for 10 min in 0.1% TritonX-100/PBS. Blocking buffer (5% BSA in 0.1% Triton/PBS) was added for 1 h, followed by incubation with BAP1 (1:500; Santa Cruz, sc-28383) and SLC7A11 (1:500; Cell Signaling Technology, 12691) antibodies overnight. Cells were washed with PBS three times and incubated with fluorescent secondary antibodies (ThermoFisher Scientific) for 2 h. The nuclei were labelled with 4′,6-diamidino-2-phenylindole (DAPI, ThermoFisher Scientific), and fluorescence was monitored using a confocal microscope (Leica).

Real-time PCR and ChIP–qPCR. Real-time PCR was conducted as previously described[60,61]. ChIP experiments were performed using a SimpleChIP Enzymatic Chromatin IP Kit (Cell Signaling Technology, 9003) according to the manufacturer's instructions. After chromatin digestion and sonication, antibodies against target proteins as well as a control antibody were used for ChIP. The enriched promoter fragments captured by antibodies were examined using real-time PCR. The signal relative to input was evaluated using a formula from the manufacturer's protocol as follows: percent input = $2\% \times 2^{(C[T]2\%\ \text{input sample} - C[T]\ \text{IP sample})}$, where C[T] = the threshold cycle of the PCR reaction. The sequences of primers used for real-time PCR and ChIP–qPCR are listed in Supplementary Table 4. The primary antibodies used for ChIP–qPCR were H2Aub (Cell Signaling Technology, 8240), RNA pol II CTD (Cell Signaling Technology, 2629), RNA pol II CTD phospho Ser5 antibody (Active Motif, 61085), RNA pol II CTD phospho Ser2 antibody (Active Motif, 61083), FOXK1 (Abcam, ab18196), FOXK2 (Bethyl Laboratories, A301–730A), HCFC1 (Bethyl Laboratories, A301–399A), OGT (Cell Signaling Technology, 5368), KDM1B (Abcam, ab193080) and ASXL1 (Santa Cruz, sc-293204).

Luciferase reporter assay. The *SLC7A11* promoter was amplified using genomic DNA extracted from UMRC6 cells and cloned into pGL3 luciferase reporter vectors. Primers used to clone around 1 kb of the promoter region of *SLC7A11* are listed in Supplementary Table 4. The luciferase reporter assay was conducted using a Dual-Luciferase Reporter Assay System (Promega, E1910) according to the manufacturer's instructions. Briefly, HEK293T cells were transfected with the appropriate plasmids for 48 h, washed with PBS, and lysed for 15 min at room temperature. Cell lysates were transferred to a 384-well plate for subsequent luciferase activity measurement. Luminescence was measured using a Gen5 microplate reader (BIOTEK).

Immunoprecipitation and western blotting. Immunoprecipitation was conducted as previously described[62,63]. Protein extracts were resolved by SDS–PAGE and transferred to a nitrocellulose membrane (Bio-Rad) using standard techniques. The primary antibodies and concentrations used for western blotting were BAP1 (1:1,000; Santa Cruz, sc-28383), SLC7A11 (1:5,000; Cell Signaling Technology, 12691), tubulin (1:5,000; Cell Signaling Technology, 2144), H2Aub (1:5,000; Millipore, 05–678), H2A (1:5,000; Millipore, ABE327), vinculin (1:10,000; Sigma, V4505), FOXK1 (1:1,000; Abcam, ab18196), FOXK2 (1:1,000; Bethyl Laboratories, A301–730A), HCFC1 (1:1,000; Bethyl Laboratories, A301–399A), OGT (1:1,000, Cell Signaling Technology, 5368), KDM1B (1:1,000; Abcam, ab193080), ASXL1 (1:1,000; Santa Cruz, sc-293204), p53 (1:1,000; Santa Cruz, sc-126), PARP (1:1,000; Cell Signaling Technology, 9542), β-actin (1:4,000; Abcam, ab8226) and V5 (1:2,000; Sigma, A8012).

Tandem affinity purification of SFB-tagged protein complexes. UMRC6 cells with stable expression of S protein, FLAG and streptavidin-binding peptide tag (SFB)-tagged BAP1 were subjected to tandem affinity purification as previously described[64]. Protein bands were excised and subjected to mass spectrometry analysis at the Taplin Mass Spectrometry Facility, Harvard Medical School. Raw mass spectrometry data were processed and further analysed using the MUSE algorithm, as previously described[64], to assign priority scores to the identified potential interacting proteins.

Xenograft model. Xenograft model experiments were performed in accordance with a protocol approved by the Institutional Animal Care and Use Committee of The University of Texas MD Anderson Cancer Center. The study is compliant with all relevant ethical regulations regarding animal research. Female 4- to 6-week-old athymic nude mice (Foxn1nu/Foxn1nu) were purchased from the Experimental

Radiation Oncology Breeding Core Facility at MD Anderson Cancer Center and housed in the Animal Care Facility at the Department of Veterinary Medicine and Surgery at MD Anderson. Cancer cell lines were resuspended on ice with PBS and the same amount of cells were injected into mice subcutaneously. tumour progression was monitored by bi-dimensional tumour measurements once a week until the endpoint. The tumour volume was calculated according to the equation $v = \text{length} \times \text{width}^2 \times 1/2$. For drug treatment experiments, 10 days after tumour cell injection, nude mice were treated with PBS or 10 mg kg^{-1} liproxstatin-1 (Sigma, SML1414) through intraperitoneal injection every two days until the endpoint, as indicated.

Histology and IHC. Xenograft tissue samples were collected and immediately fixed in 10% neutral-buffered formalin (ThermoFisher Scientific) overnight. After being washed once with PBS, samples were transferred into 70% ethanol and submitted to the Research Histology Core Laboratory at MD Anderson Cancer Center for embedding and haematoxylin and eosin staining. For IHC staining, tissue sections were processed according to methods described in our previous publications[65,66]. The antibody used for IHC was anti-4HNE (1:200, Abcam, ab46545). Images were obtained at ×400 magnification using an Olympus BX43 microscope.

Transmission electron microscopy. Xenograft tissue samples were fixed with a solution containing 3% glutaraldehyde plus 2% paraformaldehyde in 0.1 M cacodylate buffer, pH 7.3, then washed in 0.1 M sodium cacodylate buffer, treated with 0.1% Millipore-filtered cacodylate-buffered tannic acid, postfixed with 1% buffered osmium, and stained en bloc with 1% Millipore-filtered uranyl acetate. The samples were dehydrated in increasing concentrations of ethanol, infiltrated, and embedded in LX-112 medium. The samples were polymerized in a 60 °C oven for approximately 3 days. Ultrathin sections were cut using a Leica Ultracut microtome, stained with uranyl acetate and lead citrate in a Leica EM stainer, and examined with a JEM 1010 transmission electron microscope (JEOL) at an accelerating voltage of 80 kV. Digital images were obtained using an AMT Imaging System (Advanced Microscopy Techniques Corp) at the High Resolution Electron Microscopy Facility at MD Anderson Cancer Center.

ChIP–seq. ChIP was performed using the SimpleChIP Enzymatic Chromatin IP Kit (Cell Signaling Technology, 9003) following the manufacturer's instructions. Chromatin (20 µg) was incubated overnight with 5 µl H2Aub antibody (Cell Signaling Technology, 8240). Next, 100 ng fly chromatin and 0.5 µg H2Av antibody (Active Motif, 61686) were added to each tube as spike-in controls. Purified ChIP-DNA was verified on agarose gel to ensure proper fragmentation and then sent to the Sequencing and Microarray Facility at MD Anderson Cancer Center for ChIP–seq.

ChIP–seq analysis. Raw reads (single-end, 50 bp) were aligned to human reference genome hg19 using bowtie (v1.1.0), allowing up to one mismatch. Peak calling was performed using model-based analysis of ChIP–seq (MACS, v1.4.2)[67] with a cutoff of $P \leq 1 \times 10^{-8}$. Clonal reads were automatically removed by MACS. Promoter regions were defined as regions 5 kb upstream to 5 kb downstream of the TSS. The H2Aub occupancies at promoter regions were normalized as reads per kilobase per million reads (RPKMs). Fold changes and significance of H2Aub differences between conditions were determined using an MA-plot-based method with a random sampling model, which was implemented in the R package DEGseq[68]; *P* values were adjusted using the Benjamini–Hochberg method. For the average profile and heatmap around the TSS, the data matrix was generated using deepTools[69], and visualization was performed using R. The enriched binding peaks of FOXK1, AXSL1 and O-GlcNAC in HEK293T cells were collected from the GEO database with accession nos. GSM1250375, GSM1250374 and GSM1250376, respectively. The binding targets of these factors were defined as the genes whose promoter regions (3 kb upstream of TSS to 3 kb downstream of TSS) were occupied by the centre of a binding peak.

Gene expression profiling and survival analysis. RNA sequencing was performed in our previous study[34]. The differentially expressed genes on restoring *BAP1* in UMRC6 cells were defined by a cutoff of FDR < 0.05 with at least a 1.5-fold change. The expression data of *BAP1* and *SLC7A11*, patient survival data and *BAP1* mutation status in five cancer types (UVM, KIRC, KIRP, PCPG and BRCA) were obtained from TCGA, while the expression data for normal samples were from the GTEx database. All these data were generated using the UCSC Xena Browser (http://xena.ucsc.edu/). Survival analysis was conducted on the basis of *BAP1* mutation or singular or combined expression of *BAP1* and *SLC7A11*. For survival analysis with combined expression of *BAP1* and *SLC7A11*, survival was compared between two groups of patients separated by the expression of both *BAP1* and *SLC7A11* using unsupervised clustering; Group 1 had higher *BAP1* and lower *SLC7A11* expression, while Group 2 had lower *BAP1* and higher *SLC7A11* expression. The survival impact of different signatures was analysed in R using the Kaplan–Meier method with a Cox proportional hazards model.

Code availability. The software and algorithms for data analyses used in this study are all well established from previous work. All software and custom arguments are included in Methods. There is no unreported algorithm used in this paper. Results in Figs. 1, 2 and Supplementary Fig. 1 and 6b can be repeated using the source data in the Supplementary Tables. The source codes for data processing are available from the corresponding author upon reasonable request.

Statistics and reproducibility. Statistical analysis (two-tailed Student's *t*-test) was performed using R software for Figs. 1b, 2c,g,i and Supplementary Fig. 1b,f,g, and using GraphPad Prism (GraphPad Software) for other bar graphs in this manuscript. For box plots, the upper and lower edges of the box indicate the first and third quartiles (25th and 75th percentiles) of the data, and the middle line indicates the median. The whiskers extend for 1.5× the interquartile range (25–75% ranges of data) from the edges of the boxes, respectively. The fold changes and significance of H2Aub differences between conditions were determined using an MA-plot-based method with a random sampling model, which was implemented in the R package DEGseq, and the *P* value was adjusted using the Benjamini–Hochberg method in Fig. 1e,f. For GO biological process analysis in Fig. 1k, Supplementary Fig. 1h and Supplementary Table 1, the *P* value was determined by Fisher exact test, and then adjusted using the Benjamini–Hochberg method. Statistical analysis (two-tailed Student's *t*-test) was performed using R software for differential expression analysis in Supplementary Table 2. For survival analysis of the TCGA data set in Fig. 2d,j,k-n, Supplementary Fig. 6b and Supplementary Table 2, the log-rank Mantel–Cox test was carried out using R software. Pearson's correlation (two-sided) was performed to analyse gene correlation in Fig. 2b,e and Supplementary Table 2. To calculate the *P* value between groups in Figs. 4a,e,h,m,n, 6d,e-g,i,m and Supplementary Figs. 5g and 6d,e, two-way analysis of variance (ANOVA) analysis was performed. All the *P* values calculated above are indicated in the corresponding figures. Each experiment was repeated successfully more than two times with similar results, as described in the figure captions. To restore BAP1, lentivirus containing BAP1 WT and C91A coding sequence prepared in multiple independent experiments was introduced to BAP1-deficient cells separately, and similar results were found across all cell lines with successful BAP1 protein expression. To knock out or knock down genes of interest, at least two independent sgRNAs or shRNAs were employed to generate cell lines, and similar results were found in all cell lines.

Reporting Summary. Further information on experimental design is available in the Nature Research Reporting Summary linked to this article.

Data availability. ChIP–seq data supporting the findings of this study have been deposited in the Gene Expression Omnibus (GEO) under accession code GSE101987. Previously published ChIP–seq or RNA–seq data that were re-analysed here are available under accession codes GSE95097, GSM1250375, GSM1250374 and GSM1250376. The UVM, KIRC, KIRP, PCPG and BRCA data were derived from the TCGA Research Network (http://cancergenome.nih.gov/). The data set derived from this resource that supports the findings of this study is available from the UCSC Xena Browser (http://xena.ucsc.edu/). Normal sample data were derived from the GTEx database (https://gtexportal.org/home/). The data set derived from this resource that supports the findings of this study is available from the UCSC Xena Browser (http://xena.ucsc.edu/). The BAP1 genetic alterations in TCGA datasets was integrated from cBioPortal database (www.cbioportal.org), with the query of gene "BAP1" for both mutation and copy number alterations (CNA) in 5 cancer types, UVM, KIRC, KIRP, BRCA and PCPG. Following are the information of each cancer studies. One dataset for UVM: TCGA, provisional. Five datasets for KIRC: IRC, Nat. Genet. 2014; TCGA, provisional; TCGA, Nature 2013; U Tokyo, Nat. Genet. 2013; BGI, Nat. Genet. 2012. One dataset for KIRP: TCGA, provisional. Six datasets for BRCA: Sanger, Nature 2012; TCGA, Cell 2015; British Columbia, Nature 2012; TCGA, provisional; TCGA, Nature 2012; Broad, Nature 2012. One dataset for PCPG: TCGA, provisional. Source data for Figs. 1, 2 and Supplementary Fig. 1 are provided as Supplementary Table 5 'Statistics Source Data'. All other data supporting the findings of this study are available from the corresponding author upon reasonable request.

References

54. Liu, X. et al. LncRNA NBR2 engages a metabolic checkpoint by regulating AMPK under energy stress. *Nat. Cell. Biol.* **18**, 431–442 (2016).
55. Koppula, P., Zhang, Y., Shi, J., Li, W. & Gan, B. The glutamate/cystine antiporter SLC7A11/xCT enhances cancer cell dependency on glucose by exporting glutamate. *J. Biol. Chem.* **292**, 14240–14249 (2017).
56. Liu, X. & Gan, B. lncRNA NBR2 modulates cancer cell sensitivity to phenformin through GLUT1. *Cell Cycle* **15**, 3471–3481 (2016).
57. Lin, A. et al. The FoxO-BNIP3 axis exerts a unique regulation of mTORC1 and cell survival under energy stress. *Oncogene* **33**, 3183–3194 (2014).
58. Lee, H. et al. BAF180 regulates cellular senescence and hematopoietic stem cell homeostasis through p21. *Oncotarget* **7**, 19134–19146 (2016).
59. Lin, A. et al. FoxO transcription factors promote AKT Ser473 phosphorylation and renal tumor growth in response to pharmacological inhibition of the PI3K-AKT pathway. *Cancer Res.* **74**, 1682–1693 (2014).

60. Gan, B. et al. Lkb1 regulates quiescence and metabolic homeostasis of haematopoietic stem cells. *Nature* **468**, 701–704 (2010).
61. Gan, B. et al. mTORC1-dependent and -independent regulation of stem cell renewal, differentiation, and mobilization. *Proc. Natl Acad. Sci. USA* **105**, 19384–19389 (2008).
62. Gan, B., Yoo, Y. & Guan, J. L. Association of focal adhesion kinase with tuberous sclerosis complex 2 in the regulation of s6 kinase activation and cell growth. *J. Biol. Chem.* **281**, 37321–37329 (2006).
63. Gan, B., Melkoumian, Z. K., Wu, X., Guan, K. L. & Guan, J. L. Identification of FIP200 interaction with the TSC1–TSC2 complex and its role in regulation of cell size control. *J. Cell Biol.* **170**, 379–389 (2005).
64. Li, X. et al. Proteomic analysis of the human tankyrase protein interaction network reveals its role in pexophagy. *Cell Rep.* **20**, 737–749 (2017).
65. Gan, B. et al. FoxOs enforce a progression checkpoint to constrain mTORC1-activated renal tumorigenesis. *Cancer Cell* **18**, 472–484 (2010).
66. Gan, B. et al. Role of FIP200 in cardiac and liver development and its regulation of TNFalpha and TSC-mTOR signaling pathways. *J. Cell Biol.* **175**, 121–133 (2006).
67. Zhang, Y. et al. Model-based analysis of ChIP–seq (MACS). *Genome Biol.* **9**, R137 (2008).
68. Wang, L., Feng, Z., Wang, X., Wang, X. & Zhang, X. DEGseq: an R package for identifying differentially expressed genes from RNA-seq data. *Bioinformatics* **26**, 136–138 (2010).
69. Ramirez, F., Dundar, F., Diehl, S., Gruning, B. A. & Manke, T. deepTools: a flexible platform for exploring deep-sequencing data. *Nucleic Acids Res.* **42**, W187–W191 (2014).

nature research

Corresponding author(s): Boyi Gan, Wei Li

Reporting Summary

Nature Research wishes to improve the reproducibility of the work that we publish. This form provides structure for consistency and transparency in reporting. For further information on Nature Research policies, see Authors & Referees and the Editorial Policy Checklist.

Statistical parameters

When statistical analyses are reported, confirm that the following items are present in the relevant location (e.g. figure legend, table legend, main text, or Methods section).

n/a	Confirmed	
☐	☒	The exact sample size (*n*) for each experimental group/condition, given as a discrete number and unit of measurement
☐	☒	An indication of whether measurements were taken from distinct samples or whether the same sample was measured repeatedly
☐	☒	The statistical test(s) used AND whether they are one- or two-sided *Only common tests should be described solely by name; describe more complex techniques in the Methods section.*
☒	☐	A description of all covariates tested
☒	☐	A description of any assumptions or corrections, such as tests of normality and adjustment for multiple comparisons
☐	☒	A full description of the statistics including central tendency (e.g. means) or other basic estimates (e.g. regression coefficient) AND variation (e.g. standard deviation) or associated estimates of uncertainty (e.g. confidence intervals)
☐	☒	For null hypothesis testing, the test statistic (e.g. *F*, *t*, *r*) with confidence intervals, effect sizes, degrees of freedom and *P* value noted *Give P values as exact values whenever suitable.*
☒	☐	For Bayesian analysis, information on the choice of priors and Markov chain Monte Carlo settings
☒	☐	For hierarchical and complex designs, identification of the appropriate level for tests and full reporting of outcomes
☒	☐	Estimates of effect sizes (e.g. Cohen's *d*, Pearson's *r*), indicating how they were calculated
☐	☒	Clearly defined error bars *State explicitly what error bars represent (e.g. SD, SE, CI)*

Our web collection on statistics for biologists may be useful.

Software and code

Policy information about availability of computer code

Data collection	Zen (Zeiss) software was used to collect confocal images; Accuri C6 (BD Bioscience) was used to collect flow cytometry data;
Data analysis	ChIP seq analysis: R package DEGseq, bowtie v1.1.0, MACS v1.4.2. ImageJ were used for confocal images analysis; Graphpad were used for bar graphs output and statistic analysis; FlowJo_V10 was used for flow data analysis. Gene expression data were generated using the UCSC Xena Browser (http://xena.ucsc.edu/). The survival impact of different signatures was analyzed in R using the Kaplan-Meier method with a Cox proportional hazards model. The software and algorithms for data analyses used in this study are all well-established from previous work. All software and custom arguments are included in Methods section. There is no unreported algorithm used in this paper. The source code for data processing are available from the corresponding author on reasonable request.

For manuscripts utilizing custom algorithms or software that are central to the research but not yet described in published literature, software must be made available to editors/reviewers upon request. We strongly encourage code deposition in a community repository (e.g. GitHub). See the Nature Research guidelines for submitting code & software for further information.

Data

Policy information about availability of data

All manuscripts must include a data availability statement. This statement should provide the following information, where applicable:

- Accession codes, unique identifiers, or web links for publicly available datasets
- A list of figures that have associated raw data
- A description of any restrictions on data availability

ChIP-seq data that support the findings of this study have been deposited in the Gene Expression Omnibus (GEO) under accession codes GSE101987. Previously published ChIP-seq data that were re-analyzed here are available under accession code GSM1250375, GSM1250374, and GSM1250376. The UVM, KIRC, KIRP, PCPG and BRCA data were derived from the TCGA Research Network: http://cancergenome.nih.gov/. The data-set derived from this resource that supports the findings of this study is available in UCSC Xena Browser (http://xena.ucsc.edu/). The normal sample data were derived from the GTEx database: https://gtexportal.org/home/. The data-set derived from this resource that supports the findings of this study is available in UCSC Xena Browser (http://xena.ucsc.edu/). Source data for Fig. 1, 2 and Supplementary Fig. 1 have been provided as Supplementary Table 5 "Statistics Source Data". All other data supporting the findings of this study are available from the corresponding author on reasonable request.

Field-specific reporting

Please select the best fit for your research. If you are not sure, read the appropriate sections before making your selection.

☒ Life sciences ☐ Behavioural & social sciences ☐ Ecological, evolutionary & environmental sciences

For a reference copy of the document with all sections, see nature.com/authors/policies/ReportingSummary-flat.pdf

Life sciences study design

All studies must disclose on these points even when the disclosure is negative.

Sample size	No sample size calculations were performed. Sample size was determined according to our experience as well as literature reporting in terms of specific experiment.
Data exclusions	No samples or animals were excluded from the analyses
Replication	Multiple independent repeats were included for related experiments. Each experiment was performed for at least twice to make sure similar results are reproducible. ChIP-seq, RNA-Seq and mass spectormetry experiments have been done once, but ChIP-qPCR, RT-PCR and immunoprecipitation have been repeated more than twice for genes or proteins of interest.
Randomization	6-8 week female nude mice were chosen as xenograft hosts, and randomly allocated into experimental groups.
Blinding	For cell-based experiments, EM, Western blotting, immunostaining and FACS, cell types were known when prepare the samples or start to treat cells at the beginning of experiments. Data measurement for cell viability and FACS or photo capture were blinded to different person who processed assay at the time. ChIP-seq, RNA-seq and mass spectormetry analysis were blinded before analysis.

Reporting for specific materials, systems and methods

Materials & experimental systems

n/a	Involved in the study
☒	☐ Unique biological materials
☐	☒ Antibodies
☐	☒ Eukaryotic cell lines
☒	☐ Palaeontology
☐	☒ Animals and other organisms
☒	☐ Human research participants

Methods

n/a	Involved in the study
☐	☒ ChIP-seq
☐	☒ Flow cytometry
☒	☐ MRI-based neuroimaging

Antibodies

Antibodies used	H2Aub (Cell Signaling Technology, 8240), RNA pol II CTD (Cell Signaling Technology, 2629), RNA pol II CTD phospho Ser5 antibody (Active Motif, 61085), RNA pol II CTD phospho Ser2 antibody (Active Motif, 61083), FOXK1 (Abcam, ab18196), FOXK2 (Bethyl Laboratories, A301-730A), HCFC1 (Bethyl Laboratories, A301-399A), OGT (Cell Signaling Technology, 5368), KDM1B (Abcam,

ab193080), ASXL1 (Santa Cruz, sc-293204),BAP1 (Santa Cruz, sc-28383), SLC7A11 (Cell Signaling Technology, 12691), tubulin (Cell Signaling Technology, 2144), H2Aub (Millipore, 05-678), H2Aub antibody (Cell Signaling Technology, 8240), H2A (Millipore, ABE327), vinculin (Sigma, V4505), 4-Hydroxynonenal (Abcam, ab46545).p53 (Santa Cruz, sc-126), PARP (Cell Signaling Technology, 9542). tubulin (Cell Signaling Technology, 2144), β-actin (Abcam, ab8226), and V5 (Sigma, A8012). See Methods for detailed information on dilution information.

Validation

All antibodies used in our study have been validated and detailed information could be found on the website from manufactures as listed below. Some of them have also been validated by our experiments as shown in this manuscript using either over-express, knockout or knockdown strategies.
H2Aub, https://www.cellsignal.com/products/primary-antibodies/ubiquityl-histone-h2a-lys119-d27c4-xp-rabbit-mab/8240;
RNA pol II CTD, https://www.cellsignal.com/products/primary-antibodies/rpb1-ctd-4h8-mouse-mab/2629;
RNA pol II CTD phospho Ser5 , http://www.activemotif.com/catalog/details/61085/rna-pol-ii-ctd-phospho-ser5-antibody-mab;
RNA pol II CTD phospho Ser2, http://www.activemotif.com/catalog/details/61083/rna-pol-ii-ctd-phospho-ser2-antibody-mab;
FOXK1, https://www.abcam.com/foxk1-antibody-ab18196.html;
FOXK2, https://www.bethyl.com/product/A301-730A/FOXK2+Antibody;
HCFC1, https://www.bethyl.com/product/A301-399A?utm_source=Labome2018&utm_campaign=A301-399A&utm_medium=website;
OGT, https://www.cellsignal.com/products/primary-antibodies/ogt-antibody/5368;
KDM1B, https://www.abcam.com/lsd2-aof1-antibody-epr18508-ab193080.html;
ASXL1, https://www.scbt.com/scbt/product/asxl1-antibody-6e2;
BAP1,https://www.scbt.com/scbt/product/bap1-antibody-c-4?requestFrom=search;
SLC7A11,https://www.cellsignal.com/products/primary-antibodies/xct-slc7a11-d2m7a-rabbit-mab/12691;
Tubulin,https://www.cellsignal.com/products/primary-antibodies/a-tubulin-antibody/2144;
H2Aub, http://www.emdmillipore.com/US/en/product/Anti-ubiquityl-Histone-H2A-Antibody-clone-E6C5,MM_NF-05-678;
H2Aub, https://www.cellsignal.com/products/primary-antibodies/ubiquityl-histone-h2a-lys119-d27c4-xp-rabbit-mab/8240;
H2A, https://www.cellsignal.com/products/primary-antibodies/ubiquityl-histone-h2a-lys119-d27c4-xp-rabbit-mab/8240;
Vinculin, https://www.sigmaaldrich.com/catalog/product/sigma/v9131?lang=en&region=US&gclid=CjwKCAjwspHaBRBFEiwA0eM3kVN5VwVtzO3JtQWg1edd9vj8fO4qbCsSIdzANqvZtxgz0fvdsMByQBoCeTkQAvD_BwE;
4-HNE, https://www.abcam.com/4-hydroxynonenal-antibody-ab46545.html;
Actin, https://www.abcam.com/beta-actin-antibody-mabcam-8226-loading-control-ab8226.html;
V5, https://www.sigmaaldrich.com/catalog/product/sigma/v8012?lang=en&region=US&gclid=CjwKCAjwspHaBRBFEiwA0eM3kWLItkcZWmCRw30EAW5Qw3yHylAjHN_9dCRHW4NOn0xK9qrixCOJehoCf2cQAvD_BwE

Eukaryotic cell lines

Policy information about cell lines

Cell line source(s)

HEK-293T, Caki1, 786-O, 769-P, ACHN and NCI-H226 cell lines were obtained from American Type Culture Collection (ATCC). RCC4, UMRC2, SLR20, and UMRC6 cell lines were obtained from Dr. William G. Kaelin at Dana-Farber Cancer Institute. TK10 cell line was obtained from Dr. Gordon Mills at MD Anderson Cancer Center.

Authentication

Cell lines were not authenticated.

Mycoplasma contamination

All cell lines tested negative for mycoplasma contamination.

Commonly misidentified lines
(See ICLAC register)

HEK-293T cells were used to for lentiviral production and luciferase reporter assay.

Animals and other organisms

Policy information about studies involving animals; ARRIVE guidelines recommended for reporting animal research

Laboratory animals

NU/J nude female mice at 4-6 week old were purchased from ERO mouse facility in MD anderson cancer center. For Tumor xenograft models, tumor cells were injected subcutaneously into both flanks of 6-8 week old female nude mice. All animal experiments were approved by Department of Veterinary Medicine and Surgery, the university of Texas MD anderson cancer center.

Wild animals

No wild animals involved in this study.

Field-collected samples

This study didn't involve samples collected from field.

ChIP-seq

Data deposition

☒ Confirm that both raw and final processed data have been deposited in a public database such as GEO.

☒ Confirm that you have deposited or provided access to graph files (e.g. BED files) for the called peaks.

Data access links

https://www.ncbi.nlm.nih.gov/geo/query/acc.cgi?

Data access links *May remain private before publication.*	token=evavokoathgfziz acc=GSE101987
Files in database submission	C91A_H2Aub_ChIP.bw EV_H2Aub_ChIP.bw WT_H2Aub_ChIP.bw C91A_H2Aub_ChIP.fastq.gz C91A_Input.fastq.gz EV_H2Aub_ChIP.fastq.gz EV_Input.fastq.gz WT_H2Aub_ChIP.fastq.gz WT_Input.fastq.gz
Genome browser session (e.g. UCSC)	http://dldcc-web.brc.bcm.edu/lilab/jiejuns/BAP1_Gan/H2Aub_ChIP_20170515/C91A-ChIP2_subtract.bw http://dldcc-web.brc.bcm.edu/lilab/jiejuns/BAP1_Gan/H2Aub_ChIP_20170515/EV-ChIP2_subtract.bw http://dldcc-web.brc.bcm.edu/lilab/jiejuns/BAP1_Gan/H2Aub_ChIP_20170515/WT-ChIP2_subtract.bw

Methodology

Replicates	H2Aub level in the cells was verified and DNA quality was confirmed by ChIP-qPCR with appropriate control before sending for ChIP-seq. No replicates used for ChIPs-seq analysis.
Sequencing depth	Sample TotalReadsCount MappedReadsCount MappedRatio C91A-ChIP 37740545 32846643 87.03% C91A-Input 32189383 27093419 84.17% EV-ChIP 38776446 34028443 87.76% EV-Input 35778742 30024672 83.92% WT-ChIP 40504799 34956148 86.30% WT-Input 37378268 31270852 83.66%
Antibodies	H2Aub, Cell Signaling Technology, 8240
Peak calling parameters	macs14 -t alignmentA.bed -n sampleA --nomodel --nolambda -g hs --wig -S -p 1e-8
Data quality	FastQC (v0.11.2) was used for reads quality control. P < 1e-8 was used as cutoff to identify peaks with MACS (v1.4.2). sample PeakCount H2Aub_C91A 9606 H2Aub_EV 5407 H2Aub_WT 5260
Software	bowtie v1.1.0; MACS v1.4.2; deepTools v2.3.4; bedtools v2.26.0; R v3.2.3;

Flow Cytometry

Plots

Confirm that:

☒ The axis labels state the marker and fluorochrome used (e.g. CD4-FITC).

☒ The axis scales are clearly visible. Include numbers along axes only for bottom left plot of group (a 'group' is an analysis of identical markers).

☒ All plots are contour plots with outliers or pseudocolor plots.

☒ A numerical value for number of cells or percentage (with statistics) is provided.

Methodology

Sample preparation	Cells were incubated in 6-well plate containing 5μM BODIPYTM 581/591 C11 dye (Invitrogen, D3861). After incubation for 30 min, cells were washed with PBS and trypsinized followed by PI staining in PBS for 5 min. Then cells were subjected to flow cytometry analysis using a cytometer Accuri C6.
Instrument	Accuri C6 (BD Bioscience)
Software	Using Accuri C6 software to collect data and FlowJo_V10 software to analyze data.
Cell population abundance	At least 10000 cells were analyzed for each sample.
Gating strategy	Initial cell population gating (FSC-Area VS FSC-Height) was adopted to make sure doublet exclusion and only single cell was used for analysis. A figure exemplifying the gating strategy is provided in the Supplementary Table 5.

☒ Tick this box to confirm that a figure exemplifying the gating strategy is provided in the Supplementary Information.